



NTNU – Trondheim
Norwegian University of
Science and Technology

Experimental Investigation of Marine Fouling on Piles in Currents

Eirik Leikvoll Nedrebø

Marine Technology

Submission date: June 2014

Supervisor: Dag Myrhaug, IMT

Norwegian University of Science and Technology
Department of Marine Technology

Abstract

Various effects of marine fouling on piles have been addressed through a literature study and an experimental investigation. The experimental investigation was conducted on circular cylinders in steady current at subcritical Reynolds numbers. Hard marine fouling was modeled on the surface of three different cylinder models using sand and gravel particles with relative roughnesses $k/D = 0.01, 0.02$ and 0.07 . In addition, one cylinder model was kept smooth, while one cylinder model was covered with artificial fur to simulate soft marine fouling. The drag and the wake velocity were measured, and in addition a flow visualization was carried out. The cylinders had a free end and the tests were performed in a free surface flume tank.

On the cylinders covered with artificial hard marine fouling, the mean drag was found to increase with increasing surface roughness. The mean drag of a cylinder covered by artificial soft marine fouling was almost three times the drag of a smooth cylinder with the same diameter. A cylinder with a diameter of 0.042 m covered with artificial soft marine fouling, was found to have approximately the same drag as a 0.10 m smooth cylinder.

The streamwise velocity at points along the centerline of the wake was measured using the optical technique Laser Doppler Velocimetry (LDV). In the case of hard marine fouling, increasing surface roughness was found to increase the mean velocity near the cylinder, and to decrease the mean velocity further away from the cylinder. The results also indicated that increased surface roughness decreased the Reynolds number dependence of the wake closure length (the region where the mean velocity is negative).

The presence of soft marine fouling was found to have a large impact on the mean velocity in the wake. Here, the wake closure length was found to be approximately 3.6 - 3.7 times longer than for a smooth cylinder.

The flow visualization showed that the Strouhal number was reduced from approximately 0.19 to 0.16 when hard marine fouling was introduced. For soft marine fouling, the Strouhal number was approximately 0.11 . The visualization also supported the findings from the LDV tests.

It was concluded that marine fouling could have large consequences for both the forces on a circular cylinder and on the flow around it. The effects of soft marine fouling were found to be more significant than the effects of hard marine fouling for all parameters in the investigation.

Sammendrag

Gjennom en litteraturstudie og en eksperimentell undersøkelse har forskjellige virkninger av marin begroing på påler blitt adressert. Den eksperimentelle undersøkelsen ble utført på sirkulære sylindere i jevn strømming ved subkritiske Reynolds tall. Hard marin begroing ble modellert på tre forskjellige sylindremodeller med sand- og gruspartikler som hadde relative ruheter k/D på 0,01, 0,02 og 0,07. I tillegg ble en sylindremodell holdt glatt, mens en sylindremodell ble dekket av kunstig pels for å simulere myk marin begroing. Drag samt wakehastighet ble målt. Det ble også gjort en strømningsvisualisering. Sylindrene hadde en fri ende og forsøkene ble utført i en prøvetank med fri væskeoverflate.

På sylindrene dekket av kunstig hard marin begroing økte gjennomsnittlig drag med økende overflateruhet. Gjennomsnittlig drag på sylindren med myk marin begroing viste seg å være omtrent tre ganger hva som var tilfellet for en glatt sylinder med samme diameter. En sylinder med myk marin begroing med en diameter på 0,042 m, hadde omtrent samme drag som en 0,10 m glatt sylinder.

Hastigheten i strømningsretning i punkter langs wakens senterlinje ble målt ved hjelp av den optiske metoden Laser Doppler Velocimetry (LDV). For hard marin begroing ble økende overflateruhet funnet å øke middelhastigheten nær sylindren, mens middelhastigheten ble redusert i området lengre bort fra sylindren. Resultatene indikerte også at lengden av området der middelhastigheten er negativ ble mindre avhengig av Reynolds tall med økende overflateruhet.

Resultatene viste at tilstedeværelse av myk marin begroing hadde stor innvirkning på middelhastigheten i waken. Området med negativ middelhastighet ble her funnet til å være omtrent 3,6-3,7 ganger lengre enn for en glatt sylinder.

Strømningsvisualiseringen viste at Strouhals tall ble redusert fra omtrent 0,19 til 0,16 som følge av hard marin begroing. For myk marin begroing var Strouhals tall omtrent 0,11. Visualiseringen støttet også opp under resultatene fra LDV-forsøkene.

Det ble konkludert med at marin begroing kan ha store konsekvenser både for kreftene på en sirkulær sylinder og for strømmingen rundt den. Virkningene av myk marin begroing ble funnet til å være mer signifikante enn virkningene av hard marin begroing for alle de undersøkte parametrene.

Preface

This master's thesis has been written at the Department of Marine Technology at the Norwegian University of Science and Technology and presents my work over the last five months. The thesis is a continuation of my pre-project that was carried out in the fall of 2013.

Unfortunately, the extent of this thesis was limited by a couple of instruments not working properly, which considerably decreased the amount of flow parameters that could be investigated. The main experiment had to be cancelled due to this, but I hope some students in the future will carry on with the investigation. The circumstances made it a challenging job to finalize the thesis, but overall I am satisfied with the end product and certain that I have learned more from the difficulties than I would have done if everything went as planned.

First and foremost, I would like to thank my supervisors Prof. Dag Myrhaug and Ph.D. candidate Pierre-Yves Henry for their dedicated support during the semester. Having such helpful and accessible supervisors has been crucial for both the learning outcome and for the completion of this thesis. I would also like to thank fellow student Tor Huse for introducing me to the experimental facilities, Simen Strømsøyen and John Martin Godø for their support regarding the LDV, and Engineer Kristian Minde and Senior Engineer Torgeir Wahl for helping with the design of the experiments. Postdoc. Olivia Langhamer from the Department of Biology has also been very supportive, introducing me to the biological aspect of marine fouling.

Trondheim, 10 June 2014



Eirik Leikvoll Nedrebø

Contents

List of Figures	viii
List of Tables	ix
List of symbols and acronyms	x
1 Introduction	1
1.1 Objectives	3
1.2 Structure of the thesis	3
2 Theory	4
2.1 Flow around a circular cylinder	4
2.1.1 Boundary layer theory	4
2.1.2 Flow regimes at a circular cylinder	5
2.1.3 Wake velocities	8
2.1.4 Forces on a circular cylinder	9
2.1.5 Disturbances	10
2.1.6 Effect of surface roughness	12
2.2 Marine fouling	15
2.2.1 Settlement of marine fouling organisms	15
2.2.2 Types of marine fouling	17
2.2.3 Distribution of marine fouling	20
2.3 Marine roughness	21
2.3.1 Relative roughness of marine fouling	22
2.3.2 Effects of marine fouling on a structure	22
2.4 Rules and guidelines	25
2.5 Removal and control of marine fouling	26
3 Methods	27
3.1 Circulating water tunnel	27
3.2 Laser Doppler Velocimetry	29
3.3 Scaling	34
3.4 Experimental modeling of marine fouling	34
3.5 Experiment	37
3.5.1 Test setup	37
3.5.2 Cylinder models	39
3.5.3 Water level	42

3.5.4	Test procedure	42
4	Results and discussion	45
4.1	Verification of the LDV system	45
4.1.1	Convergence test	46
4.1.2	Velocities across the wake	47
4.1.3	Velocities along the wake centerline	48
4.1.4	Velocities along the span	53
4.1.5	Frequency shifting error	54
4.2	Velocity in the wake of cylinders covered by marine fouling	56
4.3	Drag coefficients	61
4.4	Flow visualization	66
5	Conclusion	69
6	Further work	71
A	Task description	I
B	Instrumentation drawings and specifications	IV
B.1	Load cell data sheet	V
B.2	Force/Torque sensor	VII
B.3	LDV brochure	XII
C	Wake velocity results	XIII
D	Circular cylinder drag coefficient	XIX
E	Drag regression analysis	XX
F	Drag time series	XXI
G	Wake visualization	XXVI

List of Figures

1.1	Monopile offshore wind turbine	2
2.1	Flow close to the separation point. From Sumer and Fredsøe (1997). (δ indicates the thickness of the boundary layer)	6
2.2	Regimes of flow around a smooth, circular cylinder in steady current. From Sumer and Fredsøe (1997)	7
2.3	Mean streamwise velocity along the wake centerline. From Norberg (1998)	8
2.4	RMS streamwise velocity along the wake centerline. From Norberg (1998)	9
2.5	Drag coefficients of circular cylinders with different relative surface roughnesses. From Achenbach (1971)	12
2.6	Drag coefficients for heavily roughened circular cylinders. From Miller (1977)	13
2.7	The Strouhal number vs. Reynolds number for circular cylinders with different relative surface roughnesses: — smooth; — · · · — $\frac{k}{D} = 75 \times 10^{-5}$; — — $\frac{k}{D} = 300 \times 10^{-5}$; — — $\frac{k}{D} = 900 \times 10^{-5}$; - - $\frac{k}{D} = 300 \times 10^{-5}$. From Achenbach and Heinecke (1981)	14
2.8	The development of marine fouling on a structure. From Langhamer (2005)	16
2.9	(a) Blue mussel, (b) Barnacles	18
2.10	(a) Kelps, (b) Hydroids	19
2.11	Definition sketch of marine roughness. From Miller (1977)	22
2.12	Drag coefficients for cylinders roughened with real marine fouling (barnacles and rust) (— $D = 0.05$ m; - - - $D = 0.10$ m; · · · $D = 0.15$ m). From Miller (1977)	24
3.1	Circulating water tunnel test section	28
3.2	Circulating water tunnel lay-out	28
3.3	The Doppler effect in the light from the laser to the moving particle. From Boutier (2012)	29
3.4	The Doppler effect in the backscattered light from the moving particle to the stationary detector. From Boutier (2012)	30
3.5	The fringe spacing in an interference pattern from two crossing laser beams. From Applied University Research, Inc. (nd)	32
3.6	2D miniLDV. From Measurement Science Enterprise Inc. (nd)	33
3.7	Simulation of soft marine fouling on marine risers, from Baarholm and Skaugset (2008)	36

3.8	Simulation of hard marine fouling on marine risers, from Baarholm (2007)	36
3.9	HBM PW4MC3 single point load cell. From HBM data sheet given in Appendix B.1	37
3.10	Test setup for the free end cylinder experiment, as seen from the side of the tank. Flow in positive x-direction	38
3.11	The five cylinder models used in the experiment	41
3.12	Water level on the connection between the load cell and the cylinder model	42
4.1	Raw signal as shown by LDV processing software. Left image shows a normal raw signal with slight noise, right image shows a sudden appearance of heavy noise	45
4.2	Convergence test at $Re = 10^4$ one diameter behind the cylinder at the wake centerline	46
4.3	Mean velocity distribution across the flow 260 mm above the lower edge of the cylinder, measured one diameter behind the cylinder at $Re = 8 \times 10^3$	47
4.4	RMS velocity distribution across the flow 260 mm above the lower edge of the cylinder, measured one diameter behind the cylinder at $Re = 8 \times 10^3$	48
4.5	Mean velocity at points along the centerline of the wake, 260 mm above the lower edge of the cylinder at $Re = 3 \times 10^3$. Comparison with Norberg (1998)	49
4.6	Mean velocity at points along the centerline of the wake, 260 mm above the lower edge of the cylinder at $Re = 10^4$. Comparison with Norberg (1998)	50
4.7	RMS velocity at points along the centerline of the wake, 260 mm above the lower edge of the cylinder at $Re = 3 \times 10^3$. Comparison with Norberg (1998)	51
4.8	RMS velocity at points along the centerline of the wake, 260 mm above the lower edge of the cylinder at $Re = 10^4$. Comparison with Norberg (1998)	52
4.9	Mean velocity distribution along the span of the cylinder, measured 1, 3 and 5 diameters behind the cylinder at $Re = 10^4$	53
4.10	Histogram comparison between empty tank velocities without and with frequency shifting on	54
4.11	Streamwise mean velocity in the wake at $Re = 10^4$ for the five cylinder models	56

4.12	Streamwise mean velocity in the wake at $Re = 5 \times 10^3$ for the five cylinder models	58
4.13	Streamwise RMS velocity in the wake at $Re = 10^4$ for the five cylinder models	60
4.14	Streamwise RMS velocity in the wake at $Re = 5 \times 10^3$ for the five cylinder models	60
4.15	Mean drag forces and drag coefficients for each cylinder	61
4.16	Standard deviations from each drag measurement time series	63
4.17	Flow visualization, Cylinders 1, 2 and 3 (in that order)	66
4.18	Flow visualization, Cylinders 4 and 5 (in that order)	67
6.1	Test rig made for the second experiment	72
6.2	The ATI IP68 Nano17 force sensor. From ATI brochure given in Appendix B.2	72

List of Tables

2.1	Height distribution of marine fouling on monopile support structures at OWEZ (Bruijs, 2010)	21
2.2	NORSOK N-003 marine fouling thickness levels	25
3.1	Circulating water tunnel specifications	27
3.2	Cylinder specifications	39
3.3	Hard marine fouling details	39
3.4	Overview of cylinder models	40
3.5	Drag measurement velocities and corresponding (smooth) Reynolds numbers	43
4.1	U_{mean}/U_{in} at selected points along the wake	57
4.2	Wake closure length l_c	59
4.3	The velocities of where heavy vibrations were first observed	62
4.4	Increase in drag coefficient caused by the presence of hard marine fouling at $Re = 9.66 \times 10^3$	64
4.5	Power law regression analysis on the drag of cylinder covered with soft marine fouling. $y = ax^m$	65
4.6	Strouhal numbers for the five cylinder models from flow visualization. $U = 0.21$ m/s	68
6.1	Specifications for the second experiment	73

Abbreviations

CWT	Circulating Water Tunnel
LDV	Laser Doppler Velocimetry
OWEZ	Offshore Windpark Egmond am Zee
RMS	root-mean-square

Nomenclature

δ	boundary layer thickness
Δt	time interval
λ	wave length
ν	kinematic viscosity
ω_n	natural frequency
ϕ	angular position on a circular cylinder
τ	wall shear stress
θ	angle between the two emitted laser beams
\vec{r}_0	laser beam index vector
\vec{V}	velocity of a particle in the flow
c	speed of light
C_D	drag coefficient
C_L	lift coefficient
C_p	pressure coefficient

D	cylinder diameter
d	fringe spacing
f	frequency received by the photodetector
f_0	emitted laser beam frequency
F_D	drag force
F_f	friction drag
F_L	lift force
F_p	pressure drag
f_p	frequency received by a moving particle
f_v	vortex shedding frequency
k	average roughness height
l_c	wake closure length
m	mass
n	index of refraction
p	cylinder surface pressure
p_∞	free stream pressure
r	cylinder radius
Re	Reynolds number
St	Strouhal number
T_0	emitted laser beam period
T_p	wave period of backscattered light

T_v	Vortex shedding period
T_i	turbulence intensity
U	incoming flow velocity
U_{in}	velocity in front of the cylinder
U_{mean}	mean wake velocity
U_{RMS}	RMS wake velocity
H	height of CWT
L	length of CWT
W	width of CWT

1 Introduction

When a structure is submerged in the ocean, marine fouling organisms will quickly settle on it. This causes the flow around the structure to be altered as compared to when it was new, which in turn among others increases the forces caused by external factors such as waves and currents. Marine fouling is a large technical, economic and environmental problem for almost all industries operating at sea, and it is crucial to understand its effects when designing, installing and operating offshore constructions. The consequences of marine fouling ranges from issues such as higher fuel costs and emissions from ships, to lower fatigue life for offshore structures or physical blockage of important systems and by concealing cracks and corrosion on a construction.

The extent of the problem can be reduced by using anti-fouling paint or by regularly inspecting and removing the marine fouling, but this can be both expensive and environmentally unfriendly. Especially the use of toxic anti-fouling paints has caused great harm to the environment over the years. Gradually, such paints have been banned from the market, and this has made surface coating more challenging and costly for the maritime industry. The development of offshore oil and gas fields, in addition to the burgeoning of the offshore wind industry in recent years has also led to an increased interest in the effects of marine fouling.

The circular cylinder is the most commonly used geometrical structure in a wide variety of offshore structures. The flow around it is therefore also the one that is most thoroughly studied and well documented (among others in comprehensive books by Sumer and Fredsøe (1997) and Zdravkovich (1997)). Also, the many variations in the flow pattern over such a fundamental geometry is believed to have sparked fascination for many researchers through the years. Investigations on the effects of surface irregularities on the surface of circular cylinders in steady currents began in the 1930s, when Fage and Warsap (1929) measured the drag on circular cylinders with different sand paper coverings. Later, among others Achenbach and Heinecke (1981) conducted similar experiments investigating the vortex shedding.

A completely different approach to marine fouling is from the ecological point of view. Obtaining data on how the flow behind a circular cylinder is affected by marine fouling could be valuable to marine ecologists for understanding the dispersal of different species.

Simulating marine fouling in a physical experiment is a challenging task, real fouling can exhibit a wide variety of shapes, sizes and physical properties, and it is therefore crucial to identify the main characteristics of some of the species. Performing experiments with marine fouling on a circular cylinder requires knowledge from several disciplines such as hydrodynamics and biology, making it a highly multidisciplinary field of study.

The focus in this thesis will be on marine fouling on piles, which are typically used as foundations for structures in relatively shallow water such as offshore wind turbines. By locating wind turbines offshore, it is possible to utilize the fact that the wind is stronger and more reliable than it is on land to generate electricity. The offshore wind turbines are usually placed in groups, called wind farms or wind parks. Figure 1.1 shows an outline sketch of a typical wind turbine with a monopile foundation. This type of foundation is used in most large scale wind farms at water depths of up to 30 m. The diameter is typically in the range 4 m to 6 m.

The first offshore wind farm was built in Denmark in 1991 (EESI, 2010), and the countries around the North Sea still dominate the market. As of 2013, there were 58 European offshore wind farms producing a total of 6040 MW in 10 different countries (EWEA, 2013). The European Wind Energy Association (EWEA, 2011) has estimated that this capacity will reach 40 GW by 2020, which will be equivalent to 4% of Europe's total energy demand.



Figure 1.1: Monopile offshore wind turbine
<http://www.theengineer.co.uk>

1.1 Objectives

The objectives of this master's thesis are as follows:

- To provide a theoretical background by performing a review of existing literature related to marine fouling and the flow around a circular cylinders such as piles
- To carry out experiments investigating how the flow around a circular cylinder in steady current and the forces on it is affected by the presence of marine fouling
- To present and analyze the results and compare them with previous findings

The investigation does not focus on the constructional details or the local conditions around certain types of pile-based structures, but rather aims to give a general assessment of the consequences of marine fouling on constructions with circular cross-sections.

The full task description as given by the supervisor is provided in Appendix A.

1.2 Structure of the thesis

The thesis consists of three main parts:

Theory, where the necessary background theory needed are established. The theory part aims to give a general description of some of the theory related to experimental investigations on the topic of marine fouling on circular cylinders, and parts of it reaches beyond what is actually investigated in this thesis.

Methods, where the experimental techniques used are described together with descriptions of the design of the experiments.

Results and discussion, where the experimental results are presented, analyzed and discussed.

2 Theory

This section provides a review of relevant theory related to flow around circular cylinders and some different aspects of marine fouling. The aim is to give an overview of the underlying hydrodynamic and biological topics necessary for designing useful and realistic experiments.

2.1 Flow around a circular cylinder

The circular cylinder can be found extensively in most offshore structures. Jacket platforms, pile-based foundations, risers and pipelines all have the circular cylinder as their central building block. A circular cylinder is characterized as a bluff body, meaning that it will experience a large region of disturbed flow around it when exposed to an incoming flow. In the following, some fundamental fluid mechanics will be described with focus on the effects this region of disturbed flow has on a circular cylinder in steady, uniform flow.

2.1.1 Boundary layer theory

As described by Schlichting and Gersten (2000), a major milestone in hydrodynamics was achieved by Ludwig Prandtl in 1904. Up until this, theoretical hydrodynamics had not been able to describe real fluid flow in practice, mainly since no practical methods of calculating the effects of viscosity existed at the time. Prandtl's approach for solving this problem was to assume that the effects of viscosity are only experienced in a narrow region near the surface of the body. This layer is termed the boundary layer, and the approach is valid for fluids with low viscosity such as air and water.

An implication of introducing viscosity is the no-slip condition. It states that the fluid particles at a solid boundary will have zero velocity relative to the boundary. The boundary layer also explains the concept of separation, where a reverse flow causes the flow to separate from the surface and significantly alter the pressure distribution. Due to Prandtl's new methods, scientists now had mathematical tools for quantitatively calculating the forces on a body in viscous flow.

2.1.2 Flow regimes at a circular cylinder

For a circular cylinder, the Reynolds number, a non-dimensional quantity describing the ratio between inertial forces and viscous forces is given as:

$$Re = \frac{UD}{\nu} \quad (1)$$

where U is the incoming flow velocity, D is the cylinder diameter and ν is the kinematic viscosity of the fluid. The Reynolds number can in most cases be considered the governing parameter for the flow around a circular cylinder.

The flow pattern around a circular cylinder changes substantially as the Reynolds number is increased from zero. The flow can be divided into different flow regimes where each has its own characteristics as explained in the following and summarized in Figure 2.2.

At Reynolds numbers of about 3 to 5, the flow will separate from the cylinder surface. This separation can be explained by looking at the pressure distribution around the cylinder. When exposed to an incoming flow, the fluid pressure in the rear part of the cylinder is increased due to the geometry of the cylinder, causing the flow to be decelerated. This causes an adverse pressure gradient. At some point, the flow close to the surface will be reversed, and this is what causes the separation. The flow region behind the cylinder after separation is called the wake.

As explained by Sumer and Fredsøe (1997), the separation results in the formation of a shear layer downstream from the separation point as illustrated in Figure 2.1.

The vorticity from the boundary layer then forms vortices with opposite signs on both sides of the cylinder, and due to small disturbances in the fluid, one of the vortices will start to grow larger than the other. This happens at a Reynolds number of about 40, and gives rise to a periodical vortex shedding from the separation points as shown in Figure 2.2c. The frequency of the vortex shedding f_v can be expressed with the non-dimensional Strouhal number:

$$St = \frac{f_v D}{U} \quad (2)$$

The Strouhal number is approximately 0.2 for a large range of Reynolds numbers.

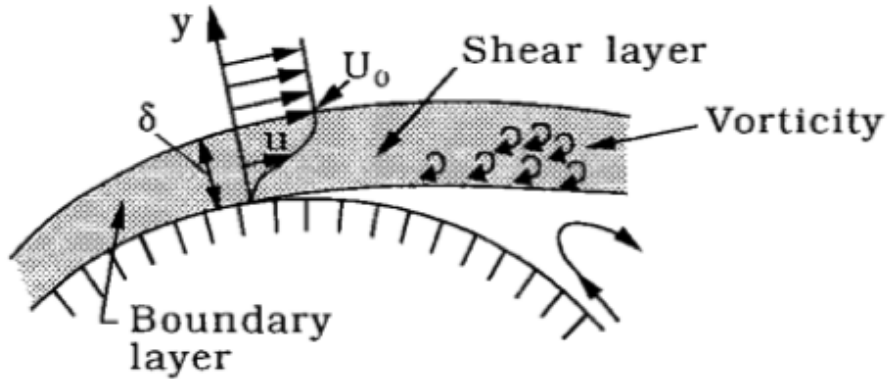


Figure 2.1: Flow close to the separation point. From Sumer and Fredsøe (1997). (δ indicates the thickness of the boundary layer)

At a Reynolds number of about 200, the wake starts to become turbulent. This turbulence develops gradually, relatively far downstream from the cylinder. As the Reynolds number is further increased, the transition to turbulence moves closer to the cylinder. The flow regime where the wake is completely turbulent, while the boundary layer remains laminar is called the subcritical regime.

For the Reynolds number range between 3×10^5 and 3.5×10^5 , in the critical flow regime, the separation points alters between being laminar and turbulent. After this, both separation points become turbulent with a partly turbulent boundary layer. This is called the supercritical flow regime.

Further increase of the Reynolds number will cause the turbulence to grow further towards the upstream side of the boundary layers. At the upper transition flow regime, which starts at a Reynolds number of approximately 1.5×10^6 , the boundary layer on one side of the cylinder is completely turbulent. Ultimately, at a Reynolds number of 4×10^6 , the boundary layer is completely turbulent and this is called the transcritical flow regime.


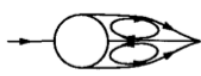



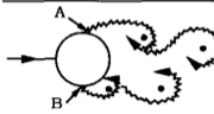
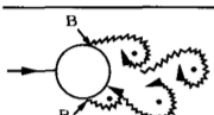
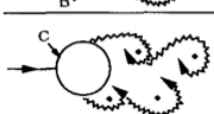

a)		No separation. Creeping flow	$Re < 5$
b)		A fixed pair of symmetric vortices	$5 < Re < 40$
c)		Laminar vortex street	$40 < Re < 200$
d)		Transition to turbulence in the wake	$200 < Re < 300$
e)		Wake completely turbulent. A: Laminar boundary layer separation	$300 < Re < 3 \times 10^5$ Subcritical
f)		A: Laminar boundary layer separation B: Turbulent boundary layer separation; but boundary layer laminar	$3 \times 10^5 < Re < 3.5 \times 10^5$ Critical (Lower transition)
g)		B: Turbulent boundary layer separation; the boundary layer partly laminar partly turbulent	$3.5 \times 10^5 < Re < 1.5 \times 10^6$ Supercritical
h)		C: Boundary layer com- pletely turbulent at one side	$1.5 \times 10^6 < Re < 4 \times 10^6$ Upper transition
i)		C: Boundary layer comple- tely turbulent at two sides	$4 \times 10^6 < Re$ Transcritical

Figure 2.2: Regimes of flow around a smooth, circular cylinder in steady current.
From Sumer and Fredsøe (1997)

2.1.3 Wake velocities

Norberg (1998) carried out detailed velocity measurements in the near wake of circular cylinders for Reynolds numbers from 1.5×10^3 to 10^4 . Figures 2.3 and 2.4 show the mean velocity and root-mean-square (RMS) velocity results from his measurements along the wake centerline. The y-axes show the wake velocity as a fraction of the incoming flow velocity and the x-axes show the number of diameters from the rear end of the cylinder.

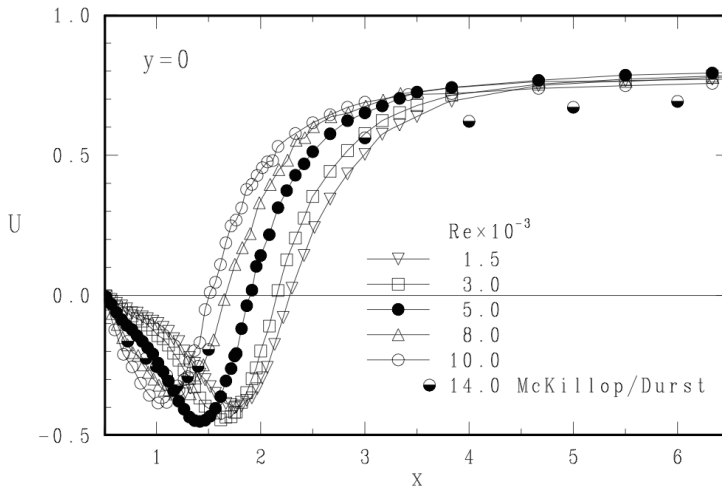


Figure 2.3: Mean streamwise velocity along the wake centerline. From Norberg (1998)

From the figures, it can be seen that the mean streamwise velocity is negative until approximately 1.5 to 2 diameters behind the cylinder, where it rapidly increases to about 3/4 of the incoming flow velocity. The RMS streamwise velocity has a peak between approximately 1 and 2 diameters from the cylinder, before it stabilizes at a velocity of about 0.2. Both values are less dependent on the Reynolds number from about 3 diameters and outwards than they are close to the cylinder.

Norberg uses the wake closure length l_c , which can be defined as the distance from the rear end of the cylinder to the point where the mean velocity is zero. Utilizing this parameter when investigating the effect of different Reynolds

numbers on the mean velocity, it can be seen that l_c is significantly reduced as the Reynolds number is increased.

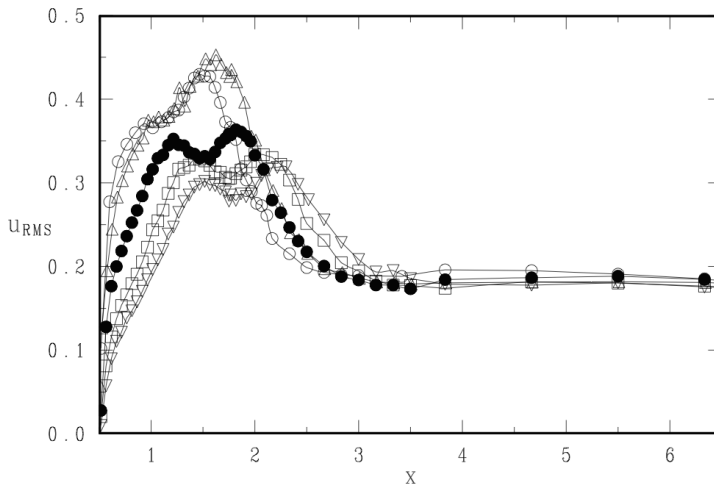


Figure 2.4: RMS streamwise velocity along the wake centerline. From Norberg (1998)

2.1.4 Forces on a circular cylinder

The drag forces on a cylinder in steady flow can be divided into two components; one from pressure and one from friction:

$$F_D = F_p + F_f \quad (3)$$

where the friction drag F_f is due to wall shear stress τ .

The pressure drag F_p is caused by the difference between the high pressure in the stagnation region in the front and the low pressure in the separated region in the rear end of the cylinder (White, 2008). The pressure coefficient is defined as:

$$C_p = \frac{p - p_\infty}{\frac{1}{2}\rho U^2} \quad (4)$$

where p is the cylinder surface pressure, p_∞ is the free stream pressure and $\frac{1}{2}\rho U^2$ is the dynamic pressure.

The pressure drag over a circular cylinder with radius r is obtained by integrating the pressure over the cylinder surface:

$$F_p = \int_0^{2\pi} p \cos(\phi) r \, d\phi \quad (5)$$

Equivalently, the friction drag is found by integrating the wall shear stress:

$$F_f = \int_0^{2\pi} \tau \sin(\phi) r \, d\phi \quad (6)$$

The drag force is often expressed non-dimensionally by the drag coefficient:

$$C_D = \frac{F_D}{\frac{1}{2}\rho DU^2} \quad (7)$$

The drag coefficient for a smooth circular cylinder is a function of the Reynolds number. It will experience a rapid drop as the flow enters the critical flow regime, and this is called the drag crisis. This phenomenon is associated with a narrowing of the wake, caused by the separation points moving downstream because of the transition to turbulence in the boundary layer in this flow regime.

Since this narrowing of the wake causes the separation points to come closer to each other, an abrupt increase in the Strouhal number is also experienced in this region.

When there is vortex shedding, there will also be a lift force component in the direction normal to the flow. The lift coefficient is expressed as:

$$C_L = \frac{F_L}{\frac{1}{2}\rho DU^2} \quad (8)$$

where F_L is the lift force.

The lift force oscillates with the same frequency as the vortex shedding frequency, while the drag force oscillates at twice the vortex shedding frequency.

2.1.5 Disturbances

In all practical cases, a system with a circular cylinder in an incoming flow will be subject to a wide range of disturbances that will influence the flow

field. When performing an experiment, it is thus important to be aware of how such disturbances will affect the end result. Previously, it was stated that the Reynolds number in most cases is the governing parameter for flow around circular cylinders. But, as pointed out by Zdravkovich (1997), if one of the disturbances become large enough, it could go from being an influencing parameter to being a governing parameter at some point.

One important example of a disturbance is turbulence. It is impossible to avoid turbulence in a practical experiment. Turbulence in the free stream will for instance alter at which Reynolds number the transition from one flow regime to another will happen. It is therefore important that the test facility used for experiments has a low free stream turbulence, and to document the magnitude of it. The turbulence intensity Ti is most commonly given as a percentage of the free stream velocity.

Many experiments on circular cylinders in water flow are conducted in water tunnels. These tunnels are enclosed by walls which cause blockage since the water is restricted from flowing sideways. The wall blockage in such tunnels is defined as the diameter-to-width ratio. The wall blockage effect can typically be ignored when the blockage ratio is below 0.1. Gap blockage is a similar influence, defined as the ratio of the gap between the cylinder and the wall, to the width of the tank.

The flow around a circular cylinder is always three-dimensional. It is often assumed that as long as the length-to-diameter ratio (the aspect ratio) is sufficiently large, the flow behaves in a completely two-dimensional manner. That is not the case, and it is important to be aware of how the aspect ratio affects the flow around the cylinder in all three dimensions. If the cylinder has one free end, the three-dimensionality of the system will be significantly increased as compared to the most common case where the cylinder is fixed at both ends to the side walls. This happens due to the formation of a secondary flow over the free end which can result in increased Strouhal number. For the free end case, the aspect ratio is expressed as the height-to-diameter ratio.

Another important disturbance which could be dominant especially at certain velocities is oscillations, which could arise from resonance behavior due to the vortex shedding frequency (or other vibrations in the facility), coinciding with any natural frequencies in the system.

In the following, an important flow disturbance parameter for this investigation will be presented more in detail, namely surface roughness.

2.1.6 Effect of surface roughness

For the case of marine fouling, the effect of surface roughness is of special interest, since the fouling could introduce significant surface irregularities on the cylinder that could disturb the flow around it.

To be able to describe these irregularities, it is useful to divide into two influencing parameters:

- Relative roughness - the ratio between the mean size of excrescences k and the cylinder diameter D
- Texture - describing the shape and distribution of the excrescences

Fage and Warsap (1929) did some of the first systematic experimental studies on the effects of surface roughness on circular cylinders. It had previously been noted that roughness generates turbulence, and the influence of surface roughness on the drag was investigated by attaching glass paper to cylinder specimens. Achenbach (1971) later measured the pressure distribution around circular cylinders in similar experiments. The drag coefficients around the critical flow regime obtained for different relative roughnesses are shown in Figure 2.5.

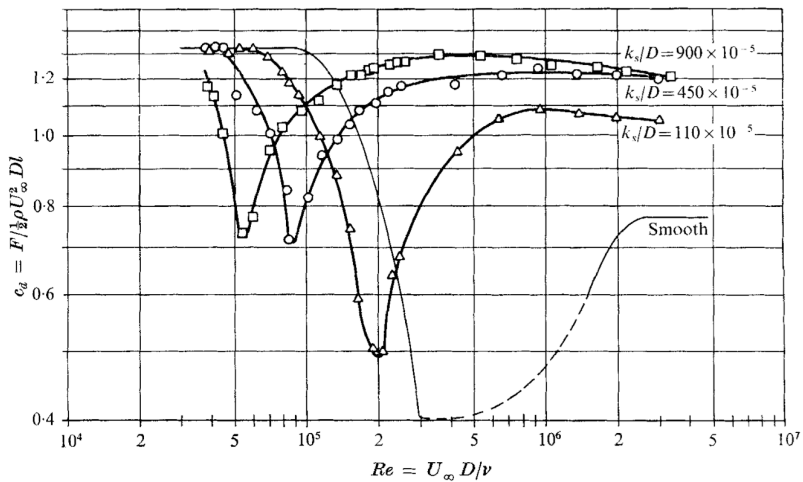


Figure 2.5: Drag coefficients of circular cylinders with different relative surface roughnesses. From Achenbach (1971)

It can be seen that a roughened cylinder will experience the drag crisis at a lower Reynolds number than a smooth cylinder. Another effect is that the roughening of the surface lowers the effect of the drag crisis, making the drop in drag coefficient lower. It is therefore evident that the drag coefficient in this flow region is not only a function of Reynolds number, but also of the surface roughness. For lower Reynolds numbers, the drag coefficient seems to approach the value of a smooth cylinder. This is supported by Miller (1977), who performed experiments on circular cylinders covered with coarse artificial roughness (See Figure 2.6).

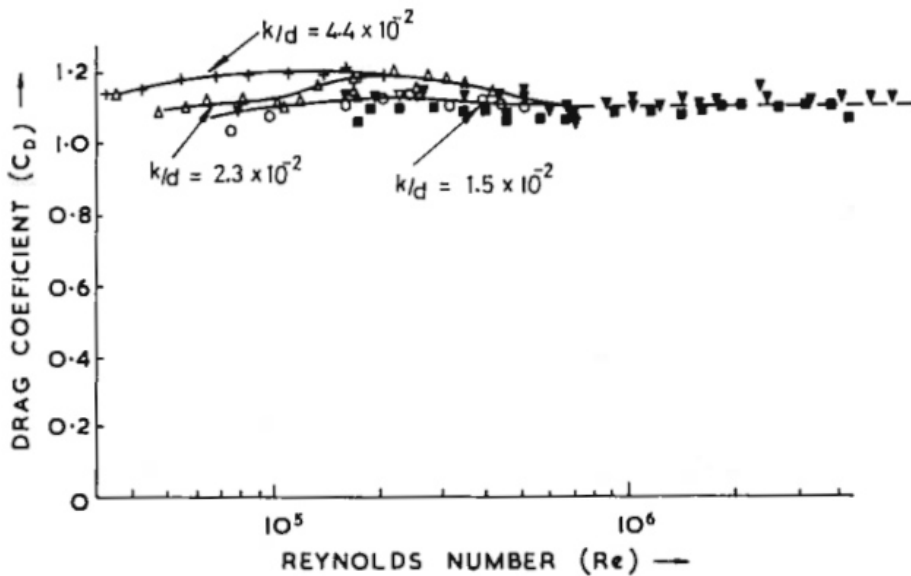


Figure 2.6: Drag coefficients for heavily roughened circular cylinders. From Miller (1977)

The physical explanation of the above-mentioned effects is that the irregularities on the cylinder forces an earlier transition to turbulence in the boundary layer. The decreased magnitude of the drag crisis due to increased roughness is related to the position of the separation points. It is known that the separation point moves to the rear end of the cylinder when turbulence is introduced in the

boundary layer. This causes a narrower wake and hence a lower drag in the critical flow regime. For a roughened cylinder, the flow is not able to stay attached to the cylinder as far as for a smooth cylinder. The wake will therefore not become as narrow as for the smooth case and hence the drop in drag coefficient will be of a lower magnitude.

It seems obvious that this change in angular position of the separation points must have an effect also on the vortex shedding. Results from experiments carried out by Achenbach and Heinecke (1981) are shown in Figure 2.7.

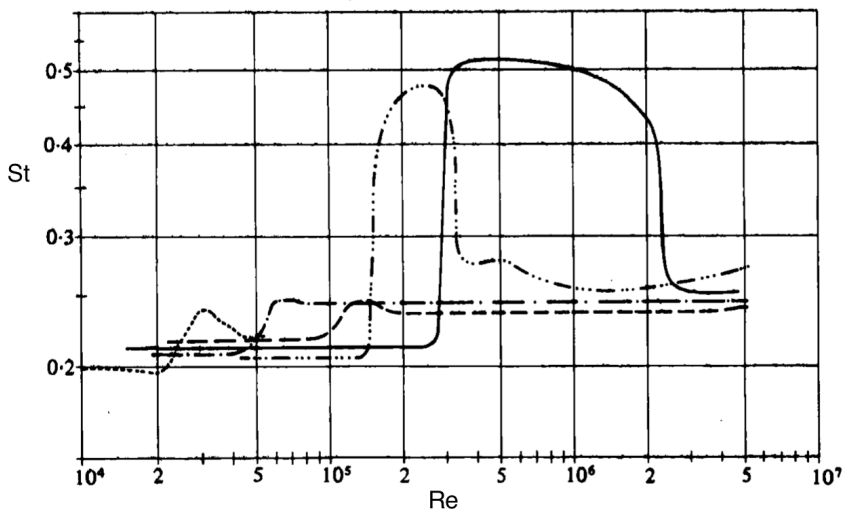


Figure 2.7: The Strouhal number vs. Reynolds number for circular cylinders with different relative surface roughnesses: — smooth; — · · · — $\frac{k}{D} = 75 \times 10^{-5}$; — — $\frac{k}{D} = 300 \times 10^{-5}$; — · — $\frac{k}{D} = 900 \times 10^{-5}$; · · · · $\frac{k}{D} = 300 \times 10^{-5}$. From Achenbach and Heinecke (1981)

As mentioned previously, the Strouhal number of a smooth circular cylinder is approximately equal to 0.2 for a wide range of Reynolds numbers, before it suddenly increases in the critical flow regime due to a narrower wake. This is illustrated by the smooth line in Figure 2.7. Since increasing the surface roughness moves the separation points further away from each other, the magnitude of the increased vortex shedding frequency will not be as significant as for the smooth

cylinder. Also the increase in vortex shedding frequency happens at a lower Reynolds number when the roughness is increased for the same reasons as for the lower Reynolds number drag crisis. From the dotted and dashed lines in Figure 2.7, the tendency seen is that an increasing surface roughness causes a gradually lower maximum Strouhal number at a gradually lower Reynolds number.

2.2 Marine fouling

Dürr and Thomason (2010) defines fouling as the accumulation of unwanted material at an interface. When the unwanted material is organisms like plants, animals and microorganisms in the interface between the water and a submerged structure, it is often termed *biofouling* or just *marine fouling* as used in this thesis. Marine fouling causes problems for nearly all industries operating in water: Offshore wind farms, which are focused upon in this study, but of course also e.g. for ships, platforms, pipe systems, aquaculture and wave power facilities. To be able to quantify different fouling organisms, it is necessary to look into some biology.

2.2.1 Settlement of marine fouling organisms

The development of marine fouling starts immediately when a structure is submerged into the ocean. The surface of the structure attracts organic material on a molecular level, that creates a conditioning film on the surface due to physical forces such as electrostatic interaction. Shortly after, an aggregate of microorganisms attach to each other through a chemical process and create what is called a biofilm on the surface of the structure (Busscher and van der Mei, 2000). This process is called microfouling, and the biofilm serves as a foundation for attachment of larger species and allows the generation of a fouling community on the structure. A schematic overview of the development process of marine fouling on a submerged structure is shown in Figure 2.8.

The reproduction and dispersal of marine fouling organisms are in many cases done by production of planktonic larvae that are transported by current to new surfaces. The environmental conditions are of importance here, among others since increased current velocity and turbulence can increase the settlement of some species and decrease the settlement of others (Koehl, 2007).

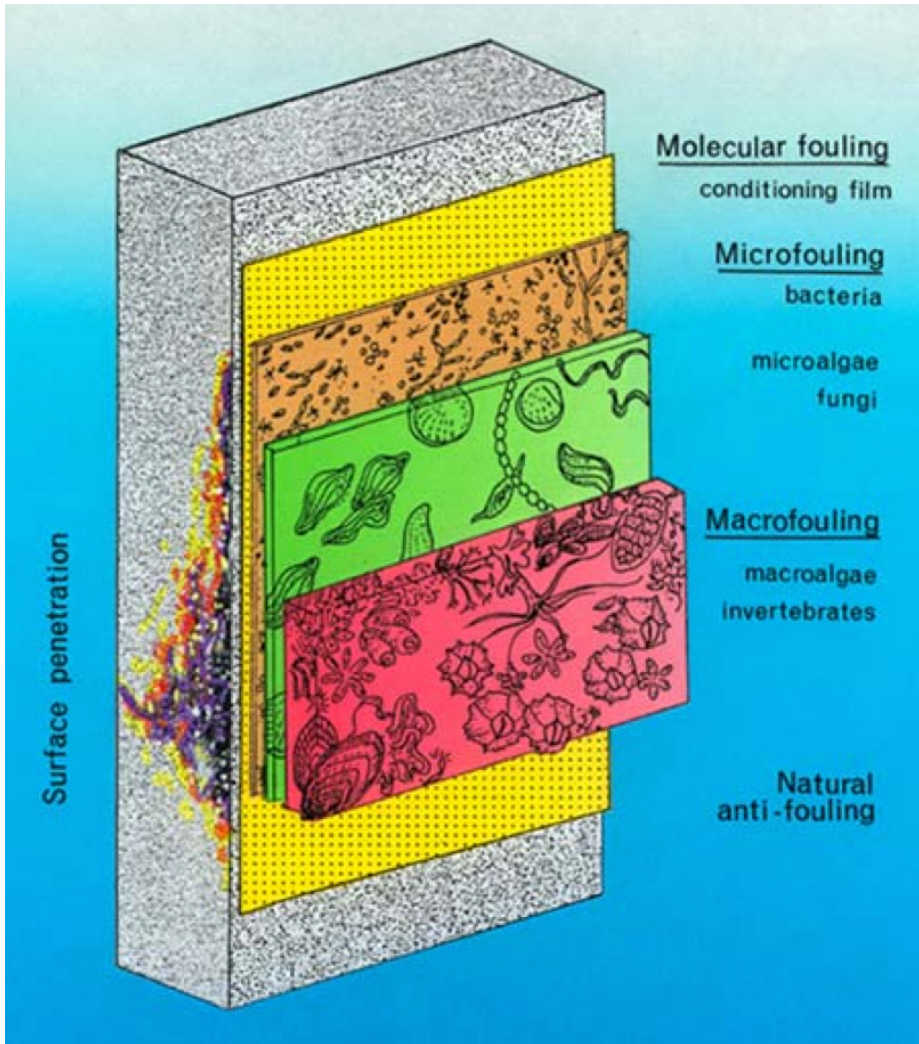


Figure 2.8: The development of marine fouling on a structure. From Langhamer (2005)

2.2.2 Types of marine fouling

Based on investigations in the North Sea, Oldfield (1980) categorized marine fouling into the following categories:

- Mussels
- Kelps
- Algae (other than kelps)
- Barnacles, tubeworms, limpets, etc.
- Hydroids, bryozoa
- Sponges, anemones, sea squirts, alcyonium
- Rock borers

It is useful to make a distinction between hard and soft marine fouling (also termed calcareous and non-calcareous fouling). In the following, the characteristics of some of the fouling organisms will be described. (Based on descriptions by Oldfield (1980), Wolfram and Theophanatos (1990), Jusoh and Wolfram (1996) and Langhamer (2010)).

Hard marine fouling:

- **Mussels**

Often a dominant species in the upper layers of a structure. The rapid-growing blue mussel (*Mytilus edulis*, shown in Figure 2.9a) is a common type of mussel in the regions around the North Sea. A survey at the Swedish west coast found that the shell length can be up to 8.5 cm. The additional thickness of the mussel biomass has in some areas of the North Sea been found to reach 8 cm after only 1-2 years, and it could reach a thickness of 20 cm after 7-8 years.

- **Barnacles, tubeworms, limpets, etc.**

A group of species that are firmly attached to the surface and often only one organism thick. They attach firmly to the structure, and in many cases they will be covered by other species. The barnacle species *Balanus balanus* (shown in Figure 2.9b), which is prevalent around the North Sea usually has a height and diameter of 2-3 cm. It is a small animal living inside a cone-shaped calcareous shell. Tubeworms (*Pomatoceros*) behave similarly.



Figure 2.9: (a) Blue mussel, (b) Barnacles
<http://www.elrincondelmalacologo.com>

Soft marine fouling:

- **Kelps**

A group of brown algae (*phaeophyceae*) with a high growth rate and long life-span (up to 15 years). They have large sized long and flapping weeds in a length range of more than 100 cm. The species are found in depths of up to 30 m, and are potentially dominant in areas without mussels. Different types of kelps are illustrated in Figure 2.10a.

- **Algae (other than kelps)**

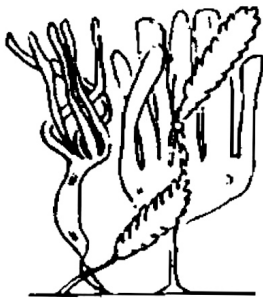
Different types of branching seaweeds of a smaller size than kelps. Occurs in the same height region as blue mussels.

- **Hydroids, bryozoa**

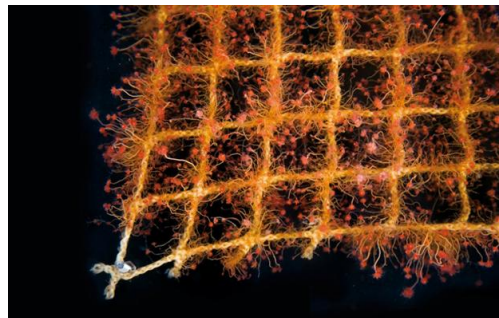
Branching and compressible flower-like growths that appear similar to seaweeds, but are in fact animals. They often grow on top of other organisms. Hydroid colonies are found in all water depths on an offshore structure, but Wolfram and Theophanatos (1990) noted that they seem to prefer dark spots such as the area beneath braces. The length of hydroids is typically about 1-2 cm, but they are easily flattened on the structure by currents. Figure 2.10b shows hydroids on a fishing net.

- **Sponges, anemones, sea squirts, alcyonium, rock borers**

Soft and often bulky organisms. Sponges are capable of boring a few millimeters into concrete while other rock borers could bore several centimeters. Anemones are usually found in depths of 15 m and downwards. They can continue to grow for up to 20 years and become as large as 35 cm in height.



(a)



(b)

Figure 2.10: (a) Kelps, (b) Hydroids

From Jusoh and Wolfram (1996) and

<http://sciencenordic.com/small-creatures-do-great-damage>

2.2.3 Distribution of marine fouling

The distribution of marine fouling is dependent on factors such as water depth, temperature, salinity, currents, waves, predation and bottom topography, and in addition the different fouling organisms are in constant competition for space, food and light (Jusoh and Wolfram, 1996). The time of the year the structure was installed also affects the distribution of the fouling (Wolfram and Theophanatos, 1990). It is essential for the success of a fouling organism that it is able to attach properly to the surface to be able to withstand the environmental forces acting on it. It is also known that species with high tolerance to wide fluctuations in environmental conditions dominate over more sensitive species and survive. Species that are able to tolerate high fluctuations in environmental conditions are known to dominate species that are more sensitive (Langhamer, 2009).

For a given area, a height distribution of the organisms can be established based on measurements of the average marine fouling thickness. Even though such height distribution statistics are available for many oil and gas platforms, the author has not found many which are relevant for structures such as offshore wind turbine piles. The platforms are usually located at larger water depths and in other geographical areas, so the results from those studies are only relevant as an indication.

However, one survey has been obtained from the Offshore Windpark Egmond am Zee (OWEZ) located off the Dutch North Sea coast (Bruijs, 2010). The survey was performed just over a year after construction in 2007, but still gives an indication on the distribution of the species. The water depth is approximately 15 m and the support structure diameter 4.6 m. The findings are summarized in Table 2.1. The results presented are based on samples and ROV observations from two coated and uncleaned monopiles.

It is noted that mussels dominate the upper depth zone, and this is also backed by other reports on North Sea fouling (e.g. Wholmersley and Picken (2003) and Oldfield (1980)). It is often termed the mussel zone. Oldfield also notes that kelps could be potentially dominant if mussels are absent.

The OWEZ survey was done after about a year in the sea. However, the fouling will change over time, and Wholmersley and Picken (2003) investigated the long-term development of fouling communities in the North Sea and found that the distribution of the fouling organisms changed significantly from year to year.

Table 2.1: Height distribution of marine fouling on monopile support structures at OWEZ (Bruijs, 2010)

Depth [m]	Thickness [mm]	Species
0-7	50-150	Mussels (<i>Mytilus edulis</i> and <i>Mytilus galloprovincialis</i>)
7-15	10-15	Hydroids and tube worms dominant. Bryozoans, barnacles, some oysters and small clusters of anemones were also observed. Less mussels.

2.3 Marine roughness

As mentioned previously marine fouling can be classified as either hard (rigid) or soft. Zdravkovich (1997) states that the roughness turbulence generated by the two types of fouling are dissimilar. If one can assume that the structure is dominated by hard marine fouling, two main effects can be considered on the cross-section of a cylinder:

- Increased cylinder diameter
- Increased surface roughness

This is illustrated in Figure 2.11, where x is the increase in diameter. It is important to note that the increased surface roughness could have a wide variety of textures when dealing with real marine fouling.

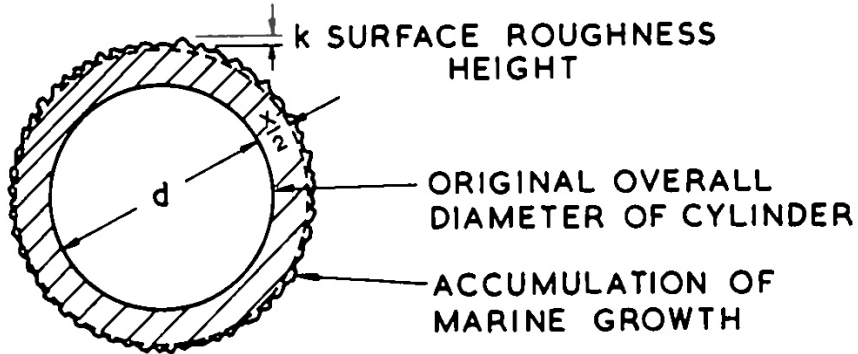


Figure 2.11: Definition sketch of marine roughness. From Miller (1977)

2.3.1 Relative roughness of marine fouling

According to Miller (1977), the typical roughness height of marine fouling is in a range from $k = 10^{-4}$ m to $k = 5 \times 10^{-2}$ m. This corresponds to relative surface roughnesses from $k/D = 2 \times 10^{-5}$ to $k/D = 10^{-2}$ for a pile of 5 m diameter. Bruijs (2010) did however estimate the average roughness height of blue mussels to be 0.1 m, which corresponds to $k/D = 2 \times 10^{-2}$ for $D = 5$ m, so coarser surfaces could be present in the mussel zone.

2.3.2 Effects of marine fouling on a structure

The presence of marine fouling will alter both the forces and the flow around a cylindrical structure. A number of the effects on the loading of a structure has been assessed by Jusoh and Wolfram (1996). Since the fouling introduces additional mass and volume to the structure, it is obvious that the displaced volume and structural loading will increase. Due to the relatively low weight of the fouling organisms, the increase in structural weight can be neglected for most structures. Blue mussels have, as previously stated been found to increase the thickness with up to 20 cm at the upper depth zones, and this will increase the wave loading.

Another effect of increased mass from marine fouling is that it changes the

natural frequency ω_n . The natural frequency of a structure is given as:

$$\omega_n = \frac{k}{m} \quad (9)$$

where k is the stiffness and m is the total mass. As the mass is increased, it is seen that the natural frequency is decreased.

The effects of increased surface roughness on a circular cylinder has been addressed previously, but it is important to consider that the increased cylinder diameter in most cases could be quite significant. The drag and lift coefficients decreases with increasing cylinder diameter (Equation (7) and (8)). At the same time, increasing surface roughness lowers the effect of the drag crisis and moves the transition to turbulence to a lower Reynolds number (from Section 2.1.6).

Similarly, the vortex shedding will also be affected. The Strouhal number is increased with increasing cylinder diameter (Equation (2)), and from Figure 2.7 it is known that the sudden increase in shedding frequency happens at a lower Reynolds number and has a lower magnitude than for a smooth cylinder. Any alterations of the vortex shedding frequency could affect the vibrations a the structure. This could have implications for the fatigue life of a structure. Also, if the vortex shedding frequency is close to one of the natural frequencies of a system (a phenomena called "lock-in"), resonance will occur and the structure could be damaged (Sumer and Fredsøe, 1997).

Miller (1977) carried out wind tunnel experiments on steel tubes with artificial and real marine roughness in a Reynolds number range from 2×10^5 to 4×10^6 . The real marine fouling was obtained by immersing the cylindrical test specimens in sea water for a period of nearly one year. After removing all soft marine fouling, the dominant fouling was tiny barnacles and rust. With cylinder diameters of 0.05 to 0.15 m, this gave a large relative surface roughness, and the drag coefficient showed almost no variation with Reynolds number as shown in Figure 2.12. If one inspect the trends from Figure 2.5 and the results from Figure 2.6, this is as expected.

As briefly mentioned previously the presence of marine fouling could also have practical implications for the operation and maintenance of an offshore structure. It can for instance restrict or block access to systems on the structure, and it can also make inspection of the integrity of structural members difficult if the member is covered with fouling.

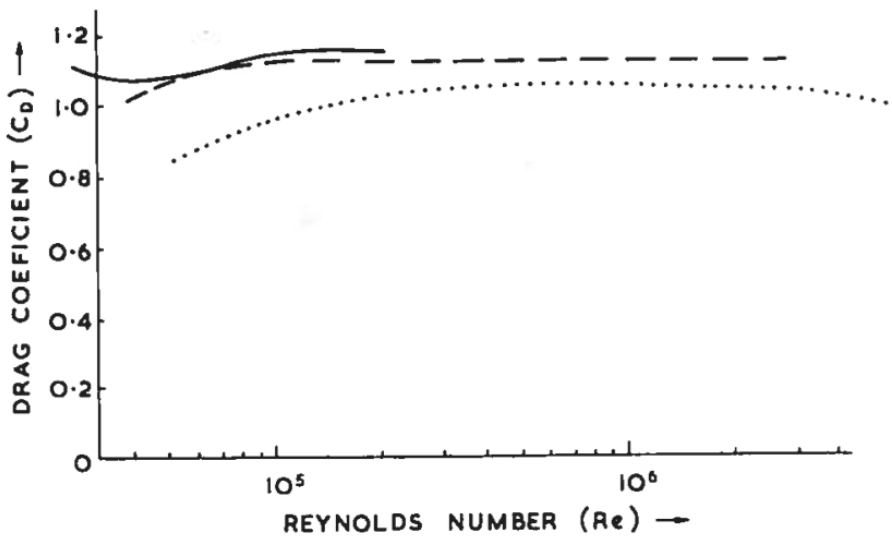


Figure 2.12: Drag coefficients for cylinders roughened with real marine fouling (barnacles and rust) (— $D = 0.05$ m; - - - $D = 0.10$ m; ··· $D = 0.15$ m). From Miller (1977)

2.4 Rules and guidelines

The ISO 19901-1 standard states that due to the large location dependence of marine fouling, site-specific studies should be performed when necessary to establish the likely thickness of the marine fouling and its depth dependence. When it comes to general design considerations, the standard states:

”Due consideration shall be given to the influence of marine growth on hydrodynamic actions during its design service life, as well as to the increased mass and its influence on dynamic response and the associated mass inertial forces.”

On the effect of marine fouling on the hydrodynamic actions, the standard further states that the influence is due to increased dimensions and roughness, and that the cross-sectional area of the structural components should be increased to account for this. Structural members located either above the highest astronomical tide or sufficiently deep for marine fouling to be sparse can be considered as hydrodynamically smooth, all other members should be considered rough.

NORSOK N-003 gives specific values for marine fouling thickness in Norwegian waters which can be used if site-specific data is not available (Table 2.2). The growth can be assumed to increase linearly to the given values for the first two years. The standard states that the roughness height should be taken as 20 mm below +2 m and the specific weight in air as 13 kN/m³ if no other data is available.

Table 2.2: NORSOK N-003 marine fouling thickness levels

Water depth [m]	56-59° N [mm]	59-72° N [mm]
+2 to -40	100	60
Under -40	50	30

2.5 Removal and control of marine fouling

Due to the large implications of marine fouling for offshore industries, there has been a large focus on developing techniques for controlling and removing it. Anti-fouling paints have been used since the mid-nineteenth century (Woods Hole Oceanographic Institute, 1952), but protecting ships from marine fouling dates as long back as the ancient times, when among others the greeks and the romans covered their vessels with wax and lead sheathing in order to reduce the marine fouling (Yebra et al., 2004).

In the early ages of modern anti-fouling paint, the paint contained toxic metals such as copper oxide, mercury oxide, lead and arsenic. By the late 1950s, the metal-based anti-fouling paints were replaced by organotin-based compounds¹ such as tributyltin (TBT). TBT proved to be remarkably efficient for anti-fouling, but unfortunately there proved to be large health and environmental issues associated with it. The way this anti-fouling paint works is that it releases small particles killing the growth that attaches to its surface. The problem is that the particles stay in the sea where they cause serious damage to the marine life. This has resulted in international regulations restricting and eventually banning the use of TBT (International Maritime Organization, 2002).

The increased focus on reducing the environmental harm caused by anti-fouling paints has forced the industry to search for new anti-fouling methods. It has proven difficult to develop effective anti-fouling products completely free of biocides, and although some promising results has emerged, the completely non-toxic universally effective anti-fouling paint is still a product of the future (Almeida et al., 2007).

In most cases, the fouling has to be removed at some points over the life-span of an ocean structure. There are several techniques for doing this, but for ships in dry-dock, sandblasting and hydroblasting are commonly used.

The marine fouling on the underwater parts of offshore structures is usually removed by divers or remotely operated vehicles equipped with mechanical tools or high-pressure water blasters. One important issue with removing the growth mechanically is that the coating of the structure could be damaged such that it becomes more prone to corrosion issues if not re-coated. For fixed offshore structures, re-coating is not a possibility, since it has to be performed in a dry environment.

¹Chemicals containing bonds between tin and carbon

3 Methods

The experimental investigations described in this thesis were conducted in the circulating water tunnel (CWT) at the Marine Technology Centre in Trondheim. The following section contains a description of the test facility, including all measurement equipment used in the experiment and a description of the test procedure.

The initial plan for this thesis was to first conduct a preliminary experiment with a basic test setup using equipment that was readily available. Then, from the experience taken from this preliminary test, a more advanced and accurate test setup was to be made. Unfortunately, it was not possible to perform the second experiment due to a broken force sensor. Therefore the original plans were adjusted during the course of the study and all results presented in this thesis are based on the preliminary experiment.

3.1 Circulating water tunnel

The CWT consists of a pump circulating water through a tunnel, and it is mainly used for student exercises and research projects. It has a transparent test section (shown in Figure 3.1) with a detachable lid which makes it possible to operate with or without free surface. The flow velocity in the tunnel is controlled by changing the pump frequency. The tunnel is equipped with LDV (Laser Doppler Velocimetry) and PIV (Particle Image Velocimetry) optical flow measurement systems. Specifications and lay-out of the CWT are shown in Table 3.1 and Figure 3.2.

Table 3.1: Circulating water tunnel specifications

All over size (L x W x H)	9.10 x 3.00 x 2.10 m
Test section size	2.50 x 0.61 x 0.61 m
Flow speed	0.03 to 1 m/s
Free-stream turbulence intensity	1 %

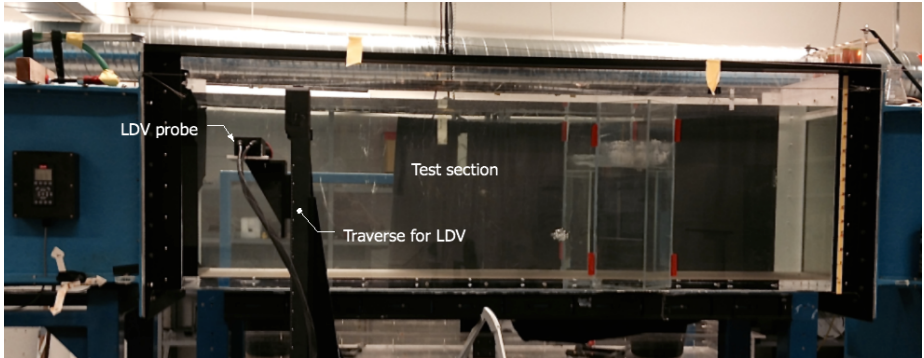


Figure 3.1: Circulating water tunnel test section

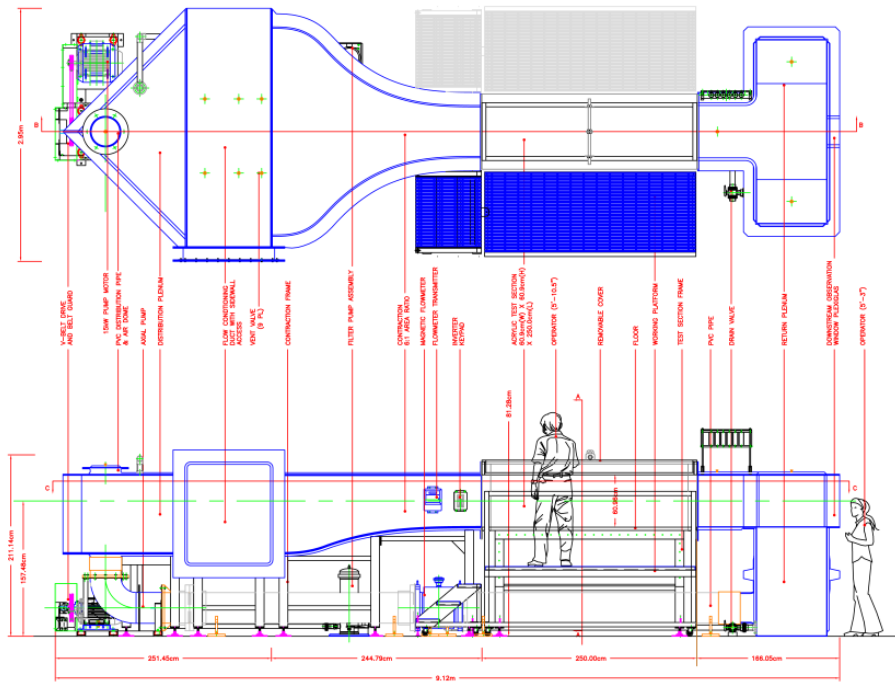


Figure 3.2: Circulating water tunnel lay-out
<http://www.ntnu.no/int/lab/circulating-water-tunnel>

3.2 Laser Doppler Velocimetry

Laser Doppler Velocimetry (LDV) is a flow velocity measurement technique well suited for use in the CWT. The method is in practice non-intrusive, and can be used for measuring the velocity at a single point in the flow. LDV is based on the principle that the frequency of incoming light is changed when a moving particle crosses it due to the Doppler effect, and this change in frequency is used to calculate the particle velocity (Boutier, 2012). In the following, the basic formulas needed for understanding the technique are derived.

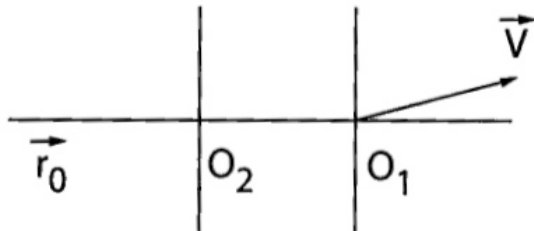


Figure 3.3: The Doppler effect in the light from the laser to the moving particle. From Boutier (2012)

The main components of an LDV system are a laser and a photodetector. The laser emits light with a frequency f_0 , and since the particle is in motion the frequency received by the particle f_p is not the same as f_0 . Figure 3.3 illustrates the unit vector \vec{r}_0 which the emitted laser beam propagates along in a medium. The distance between two successive wave fronts O_1 and O_2 in the medium, i.e. the wavelength is given by:

$$\lambda = \frac{\lambda_0}{n} = \frac{c}{nf_0} = \frac{cT_0}{n} \quad (10)$$

where n is the index of refraction, c is the speed of light and T_0 is the period of radiation (in vacuum).

During a time interval Δt , the moving particle has traveled at a velocity \vec{V} between the two wave fronts O_1 and O_2 . The distance traveled by O_2 during Δt is equal to the wavelength, plus the distance traveled by the particle during Δt along \vec{r}_0 :

Here, $S'O$ can be seen as what the distance from S' to O would have been if \vec{V} were 0, and $\overline{S'S''}$ as the distance change due to particle motion.

After one wave period T_p the second wave front S'' is emitted. After a time t , it passes the point O'' . The distance $\overline{S''O''}$ is given by:

$$\overline{S''O''} = \frac{(t - T_p) c}{n} \quad (15)$$

Now, the wavelength seen by the photodetector at O is given by the distance $\overline{O''O}$:

$$\begin{aligned} \overline{O''O} &= \overline{S'O} - \overline{S'O''} = \overline{S'O} - \overline{S'S''} - \overline{S''O''} \\ &= \frac{t c}{n} - T_p (\vec{V} \cdot \vec{r}_d) - \frac{(t - T_p) c}{n} \\ &= T_p \left(\frac{c}{n} - (\vec{V} \cdot \vec{r}_d) \right) = \frac{c}{f n} \end{aligned} \quad (16)$$

where f is the frequency received by the photodetector. By combining Equations 12 and 16, and assuming the ratio $\frac{\vec{V}}{c}$ to be very small, the following equation for the detected frequency is obtained:

$$f = f_0 \frac{1 - \frac{(\vec{V} \cdot \vec{r}_0) n}{c}}{1 - \frac{(\vec{V} \cdot \vec{r}_d) n}{c}} \approx f_0 \left(1 - \frac{\vec{V} \cdot (\vec{r}_0 - \vec{r}_d) n}{c} \right) \quad (17)$$

This proves that it is possible to measure the velocity in a fluid from the detected frequency. There are several ways of achieving this, but the most commonly used technique is called fringe velocimetry. By crossing two monochromatic and coherent laser beams at a point in the flow, a small region with light interference is created (the two laser beams are usually created by splitting a single beam). This region is called the probe volume. As particles² in the flow crosses the probe volume, light will be reflected only in regions with constructive interference. The reflected light is detected by a photodetector where the signal is detected as a sinusoid. The speed V is a function of the spacing between each interference line

²To be able to get sufficient reflection of the laser beams, small particles often have to be added in the water. This is called seeding.

(called fringe spacing, defined in Figure 3.5) d and the intensity of the reflected frequency f .

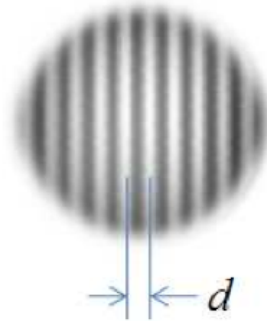


Figure 3.5: The fringe spacing in an interference pattern from two crossing laser beams. From Applied University Research, Inc. (nd)

$$V = d \cdot f \quad (18)$$

where the fringe spacing d can be found by a simple geometric consideration (see Efundu website (nd)) as:

$$d = \frac{\lambda_0}{2n \sin(\frac{\theta}{2})} \quad (19)$$

where θ is the angle between the two laser beams. The frequency f is usually obtained by running a Fast Fourier transform (FFT) algorithm on the detected sinusoid signal.

The reason for using the fringe method is that the backscattered frequencies (f) are independent of the direction of observation (\vec{r}_d), and they are in a range where photodetectors are sensitive.

The advantage of LDV, in addition to it being non-intrusive, is that it gives a quick response – making it suitable for measuring rapid changing flow phenomena such as turbulence (Steen, 2012). Another advantage is that the setup is usually

quite simple, and in practice most LDV systems do not require any calibration since the velocity is just dependent on the fringe spacing as explained above.

The CWT is equipped with a 2D miniLDV from Measurement Science Enterprise, Inc shown in Figure 3.6. The LDV is mounted on a remotely controlled and programmable traversing system which allows for precise positioning of the probe. The 2D miniLDV sensor is able to measure velocities from 1 mm/s to 300 m/s with an accuracy of 99.7% and a repeatability uncertainty of 0.1% (Measurement Science Enterprise Inc., 2013).



Figure 3.6: 2D miniLDV. From Measurement Science Enterprise Inc. (nd)

The 2D miniLDV system is also capable of measuring the direction of the flow, i.e. it can be used for measuring both positive and negative velocities. This is achieved by using "frequency shifting", which basically means that the two crossing laser beams have different frequencies and the interference fringes will move at the shift frequency. Now the direction of the flow can be determined, since the particle velocity is measured relative to the fringe velocity. There are three main methods of shifting the frequency; electro-optic, acousto-optic and mechanical systems. The 2D miniLDV uses a mechanical system. A brochure with the specifications of the LDV system is provided in Appendix B.3.

3.3 Scaling

To be able to achieve similarity when scaling from full scale to model scale, the following three similarity requirements must be met (Steen, 2012):

- Geometric similarity
- Kinematic similarity
- Dynamic similarity

Geometrical similarity is achieved if the model scale structure has the same shape as the full scale structure. If the ratios between the velocities in model and full scale are equal, kinematic similarity is achieved. This ensures that the fluid streamlines are scaled properly. To achieve dynamic similarity, the ratio between all force contributions in model and full scale has to be constant.

Full dynamic similitude between model scale and full scale is not possible to achieve. In practice it is only possible to get a constant force ratio for two force components (Frostick et al., 2011). It is therefore important to identify the governing force in addition to inertia to use for scaling. For instance, if viscous forces are of importance, the ratio between the inertial forces and the viscous forces, i.e. the Reynolds number, should be used as the similitude law.

In a model scale experiment with marine fouling on a circular cylinder, geometric similarity requires the relative roughness k/D to be constant. In addition, the shape of the irregularities has to be similar in model scale and full scale.

Using the Reynolds number as a similitude requirement for model scale tests in the CWT is in most cases not possible due to size and flow velocity limitations of the test facility. The experimental studies therefore have to focus on investigating the flow phenomenas within the allowable Reynolds number range, and use the results as indications on how the flow and forces will act at other scales.

3.4 Experimental modeling of marine fouling

In a model scale experiment it is necessary to simulate real marine fouling using artificial roughness. By covering the surface of the test specimen with different artificial materials, it is possible to obtain a relative roughness corresponding to full scale. Sand paper and sand/gravel particles have often been used for simulating hard marine fouling in model scale, under the assumption that

the relative surface roughness is the only influencing parameter. For drag measurement, this assumption is supported by Miller (1977), who carried out full scale measurements of circular cylinders covered with barnacles and rust:

"The influence of rigid marine growth upon the drag of circular cylinders in steady uniform flows is substantially the same as that of sand roughness of the same physical size"

However, the texture of barnacles is quite different as compared to for instance mussels, and it could well be that the texture is of greater importance for other fouling organisms. Miller did not carry out any experiments investigating vortex shedding or other flow phenomena, and it is possible that the impact of texture could be greater there.

If the texture of the marine fouling is to be taken into consideration in an experiment, particles such as sand and gravel would most likely prove to be inadequate. One way of achieving a similar shape and distribution as for real marine fouling is to glue particles in correct geometric scale onto the surface of the test specimens. Soft marine fouling such as algae could be modeled by covering the test specimen with a fabric, for instance a carpet with a yarn length corresponding to the size of the growth. Figure 3.7 shows a marine riser with strakes covered with a carpet in an experiment performed by MARINTEK in Trondheim (Baarholm and Skaugset, 2008). Figure 3.8 shows modeling of hard marine fouling by glueing particles to the surface from the same experiment.

In the experiments presented in this thesis, the hard marine fouling has been modeled using sand grains of different sizes. The roughness has been quantified using only the grain size of the sand, and the texture has not been taken into account. The small physical size of the test section in the CWT did not allow for cylinders large enough to make it practically achievable to use artificial fouling with specific textures. However, the sand grains used were non-uniform and irregular in size within a given interval, which would also be the case for real marine fouling. The roughness on all the test cylinders were evenly distributed and the coverage close to 100 %.



Figure 3.7: Simulation of soft marine fouling on marine risers, from Baarholm and Skaugset (2008)



Figure 3.8: Simulation of hard marine fouling on marine risers, from Baarholm (2007)

3.5 Experiment

3.5.1 Test setup

The aim of the experiment was to obtain measurements of the drag force and the wake velocity for different cylinder models covered with artificial marine fouling. In addition, flow visualizations were to be carried out using fluorescent dye. The setup consisted of an aluminum frame which was mounted in the CWT in a way that made it easy to change the cylinder specimens. The frame was made of stiff aluminum rods and efforts were made to achieve as stiff a system as possible.



Figure 3.9: HBM PW4MC3 single point load cell. From HBM data sheet given in Appendix B.1

The cylinder had one free end, and was connected to the frame via a HBM PW4MC3 single point load cell (shown in Figure 3.9) with a maximum capacity of 3 kg. The load cell was aligned to measure the streamwise forces, i.e. the drag forces. Oscillating forces from vortex shedding were too small to be registered with this setup. The load cell was connected to a computer via an A/D converter where the drag time series were saved. The load cell data sheet can be found in Appendix B.1.

The LDV was positioned on the side of the tank and was used for wake velocity measurements. A drawing of the experimental setup is given in Figure 3.10.

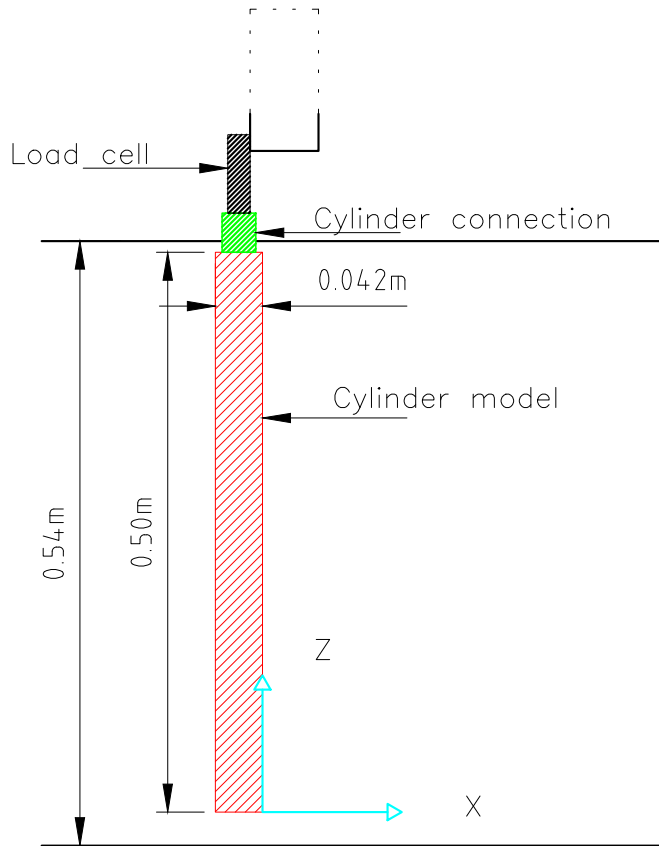


Figure 3.10: Test setup for the free end cylinder experiment, as seen from the side of the tank. Flow in positive x-direction

3.5.2 Cylinder models

Five cylinder models with the same main dimensions were used in the experiment, one smooth cylinder for reference, and four cylinders covered with different types of artificial roughness. For simplicity, the cylinders are henceforth referred to as Cylinders 1-5, where 1 is the smooth reference cylinder and Cylinders 2-5 are the roughened cylinders. The specifications for the cylinder models are shown in Table 3.2.

Table 3.2: Cylinder specifications

Diameter [mm]	42
Length [mm]	500
Wall Thickness [mm]	3
Aspect ratio (L/D)	11.9
Material	Steel

Three of the cylinders were covered by sand of different grain sizes, to simulate hard marine fouling. The sand used in the experiment were sand intended for domestic aquaria. This type of sand was found most suited since the sand had evenly distributed grain sizes. Another advantage was the wide range of grain sizes available. The chosen grain sizes represent the roughest part of the relative roughness range given in Section 2.3.1. The cylinder models could therefore be a good representation of e.g. blue mussels on an offshore wind turbine pile, or barnacles on a smaller pile. The grain sizes were controlled using sieves, and are thus given as intervals. Table 3.3 shows the details of the sand covered cylinders. The approximate average grain sizes are taken as the middle value of the interval.

Table 3.3: Hard marine fouling details

Cyl. nr.	Grain size (μm)	Avg. grain size (μm)	Relative roughness k/D
2	355-500	427.5	0.01
3	800-1000	900	0.02
4	2000-4000	3000	0.07

When modeling soft marine fouling, it was desirable to find a material that behaved similar to real long soft marine fouling. After some trial and error, a type of artificial fur was found to be best suited. It was made out of synthetic fibers (42 % modacrylic, 42 % polyacrylic, 16 % polyester), and had an average fiber length of approximately 30 mm. The fibers were attached to a textile which added approximately 0.9 mm to the cylinder diameter³. This cylinder is referred to as Cylinder 5. The cylinders are shown in Figure 3.11, and a complete list of the cylinder models can be found in Table 3.4.

Table 3.4: Overview of cylinder models

Cylinder 1	Smooth reference cylinder
Cylinder 2	Fine grained sand
Cylinder 3	Medium grained sand
Cylinder 4	Coarse sand
Cylinder 5	Artificial fur

³The additional cylinder diameter from the textile was estimated using a digital caliper



Figure 3.11: The five cylinder models used in the experiment

3.5.3 Water level

An important issue to consider in the free-end experiment was generation of waves. It was desirable to reduce the amount of waves generated by the cylinder models as much as practically possible, and this was done by visually inspecting the effects of small alterations of the water level in the tank. Since the connection in the top of the cylinder had a smaller diameter ($D = 0.03\text{ m}$) than the cylinder model, it proved most suited to have the water level just above the connection, as shown in Figure 3.12. This gave a total water level in the tank of 0.54 m. Note that the small water column just above the cylinder has not been accounted for when estimating the drag coefficient of the cylinder models.

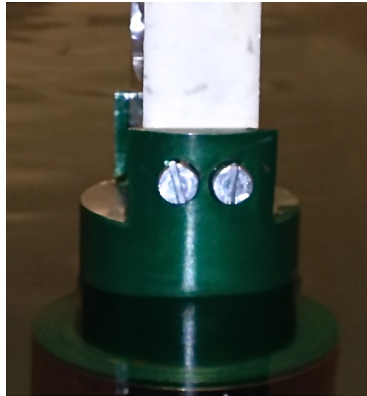


Figure 3.12: Water level on the connection between the load cell and the cylinder model

3.5.4 Test procedure

Prior to the drag measurements, the load cell was tested by applying a known weight to confirm that it gave correct measurements. A zero setting was performed after each cylinder model change. The incoming flow velocity was set by adjusting the pump frequency, where the lowest pump frequency used was 2.15 Hz. Ten different incoming flow velocities were used, with an interval of 2.15 Hz between each measurement. Table 3.5 shows the velocities measured and the corresponding smooth cylinder Reynolds number. The velocities were

Table 3.5: Drag measurement velocities and corresponding (smooth) Reynolds numbers

Velocity [m/s]	Re
0.058	2.16×10^3
0.104	3.84×10^3
0.158	5.81×10^3
0.210	7.73×10^3
0.262	9.66×10^3
0.313	1.15×10^4
0.365	1.34×10^4
0.412	1.52×10^4
0.472	1.74×10^4
0.526	1.94×10^4

obtained using LDV (without frequency shifting) in front of the cylinder. Time series of one minute were gathered for every velocity and cylinder.

Before the LDV wake measurements, a thorough investigation of the velocity results on a smooth cylinder was carried out, where the following measurements were taken for comparison with previous findings:

- Convergence test, from where the time series length were decided
- Velocities across the wake
- Velocities along the wake centerline
- Velocities along the span of the cylinder

In the first part of the LDV investigation, the system was programmed to measure the flow velocity at four points in the wake for three minutes. The points chosen were located 5, 15, 25 and 35 cm downstream from the cylinder at a vertical position of $z = 273$ mm.

After investigating the results, and due to noise issues (described in Section 4.1), it was decided to carry out some additional measurements.

The second test therefore aimed to obtain data from a large range of measurement points, and filter out the points with low data rate and/or signal-to-noise ratio (SNR). 32 points along the wake at the same vertical position as for the first tests

were investigated. The points ranged from approximately 0.5 to 8 diameters downstream from the cylinder, and each point was measured for three minutes. In this test, the velocities measured corresponded to Reynolds numbers for the smooth cylinder of 5×10^3 and 10^4 , i.e. approximately 0.136 and 0.271 m/s.

In addition to this, the wake of all five cylinder models were visualized using fluorescent dye. This was done only at an incoming velocity of 0.210 m/s ($Re = 7.73 \times 10^3$). The dye was conveyed through a nozzle that was hand-held in front of the cylinder. The visualization was recorded by a camera located beneath the transparent test section.

4 Results and discussion

4.1 Verification of the LDV system

When setting up the LDV system, it was noticed that the raw signal gave a relatively noisy signal. The raw signal shows the received signal when the laser is not activated, i.e. the signal between the probe and the computer. The noise seemed to appear randomly and with sudden peaks in the amplitude. The source of this noise was not found, and because of the randomness it was difficult to predict if the noise had appeared during one specific measurement. A common way of dealing with constant noise in the raw signal is to set a frequency threshold just above the highest peak in the signal, but this is obviously not possible in a scenario as shown in the right image of Figure 4.1.

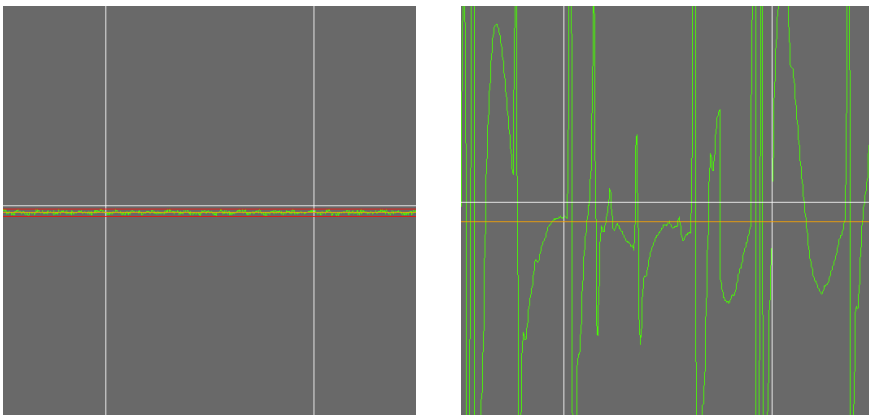


Figure 4.1: Raw signal as shown by LDV processing software. Left image shows a normal raw signal with slight noise, right image shows a sudden appearance of heavy noise

To verify the results obtained by the LDV, a series of test runs with a smooth cylinder were conducted and compared with previous results. In addition, these tests were important for investigating disturbances, especially related to the free end and the free surface in the setup. Only the streamwise velocity was measured.

4.1.1 Convergence test

Before any test runs were started, it was necessary to get an indication of how long each time series had to be. In this test, the velocity was measured in the wake centerline two diameters behind the cylinder, at a point 260 mm above the lower edge of the cylinder. The test was performed at a Reynolds number of 10^4 , and the results for the mean and RMS velocities are shown in Figure 4.2. Individual time series of 30, 45, 60, 120 and 180 seconds were conducted. The figure shows that the difference in both mean velocity and the RMS velocity for different time series lengths are within a range of < 0.015 m/s, and this shows that even for a short measurement time, it is possible to achieve acceptable results. In the following LDV verification tests, one minute time series have been used since it seems to be enough for obtaining a good indication of the flow behavior. For the main experiment, the length used is three minutes.

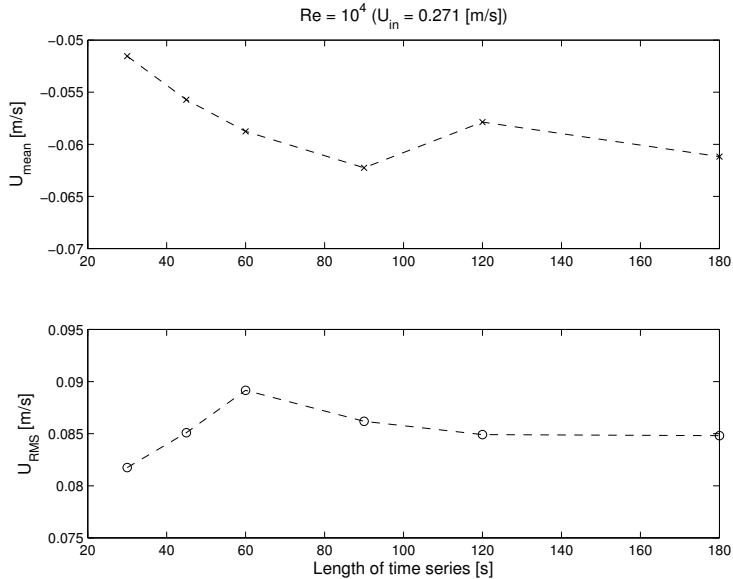


Figure 4.2: Convergence test at $Re = 10^4$ one diameter behind the cylinder at the wake centerline

4.1.2 Velocities across the wake

The first test aimed to check if the velocities across the flow were consistent with reference data. The velocities were measured one diameter behind the cylinder, at a vertical position 260 mm above the lower edge of the cylinder. The results for the mean velocity are plotted in Figure 4.3, together with previous findings by Norberg (1998). The results show that there is a slight deviation from Norbergs results, but this could be due to differences in the test setup. Norberg did his measurements in a closed test section with an aspect ratio of 65, while this experiment was conducted with a free surface and an aspect ratio of 11.9. The mean velocity measurements were also used for confirming the horizontal alignment of the probe, since that is the position with the lowest mean velocity. This position had previously been determined visually.

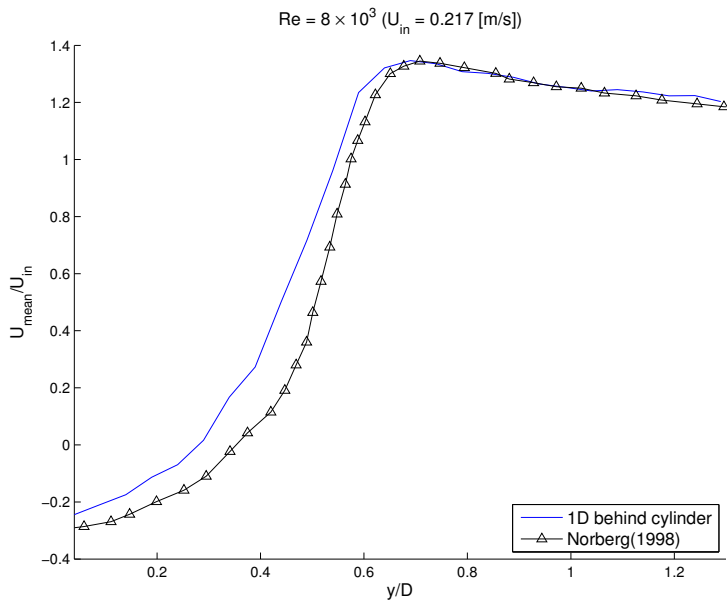


Figure 4.3: Mean velocity distribution across the flow 260 mm above the lower edge of the cylinder, measured one diameter behind the cylinder at $Re = 8 \times 10^3$

Figure 4.4 gives the RMS velocity from the same measurement, together with Norbergs reference values. Although the measured velocities show the same

trend as the reference values, the deviation is large from 0.5 diameters and outwards. Also, the highest peak is significantly lower than the reference value.

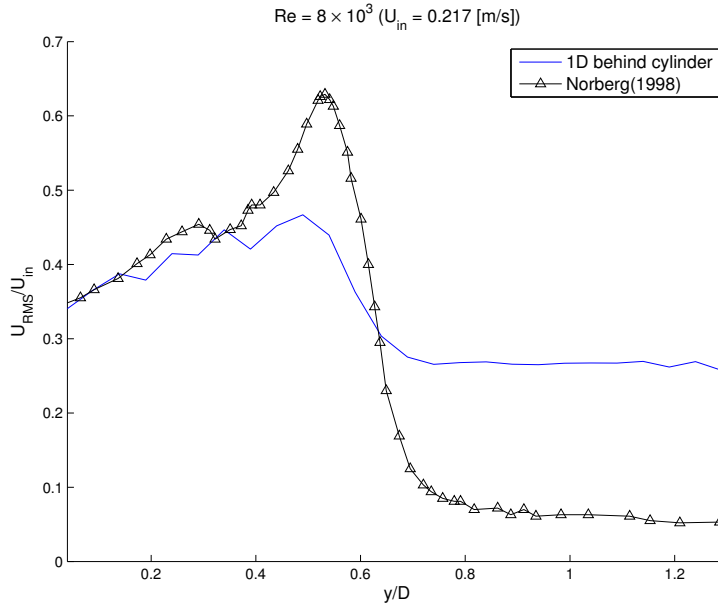


Figure 4.4: RMS velocity distribution across the flow 260 mm above the lower edge of the cylinder, measured one diameter behind the cylinder at $Re = 8 \times 10^3$

4.1.3 Velocities along the wake centerline

In the second test run the velocity was measured at selected points along the centerline in the wake of the cylinder. Figures 4.5 and 4.6 show the measured mean velocities compared with reference values for $Re = 3 \times 10^3$ and $Re = 10^4$, respectively. The figures show the same trend, but the numeric values deviate from the reference values – especially for the lowest Reynolds number.

The RMS velocities at the same points are plotted in Figures 4.7 and 4.8. $Re = 10^4$ (in Figure 4.8) gives the same trend as in Figure 4.4; the RMS velocities correspond quite well close to the cylinder, but further away the values are significantly higher. Another trend seen from Figures 4.6 and 4.8 is that

the points seem to be shifted about 0.2 diameters downstream as compared to Norberg (1998).

The RMS velocities at $Re = 3 \times 10^3$ (In Figure 4.7) are far off the reference values. It indicates that the LDV becomes less capable of providing correct measurements as the velocity is reduced. The same conclusion can be drawn from the mean velocities, as the data is closer to Norberg (1998) at the highest Reynolds number.

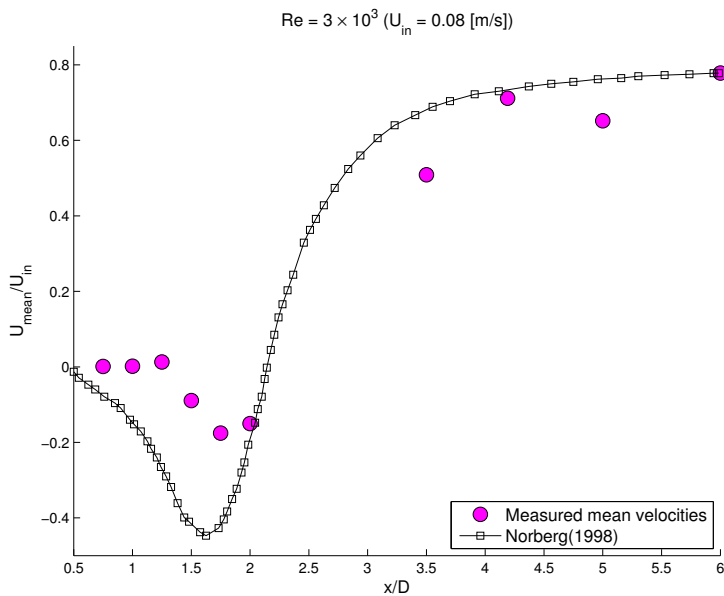


Figure 4.5: Mean velocity at points along the centerline of the wake, 260 mm above the lower edge of the cylinder at $Re = 3 \times 10^3$. Comparison with Norberg (1998)

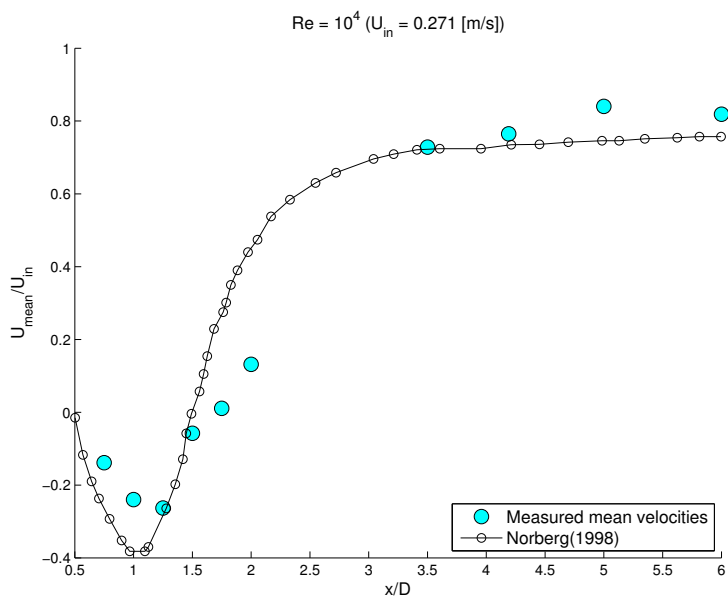


Figure 4.6: Mean velocity at points along the centerline of the wake, 260 mm above the lower edge of the cylinder at $Re = 10^4$. Comparison with Norberg (1998)

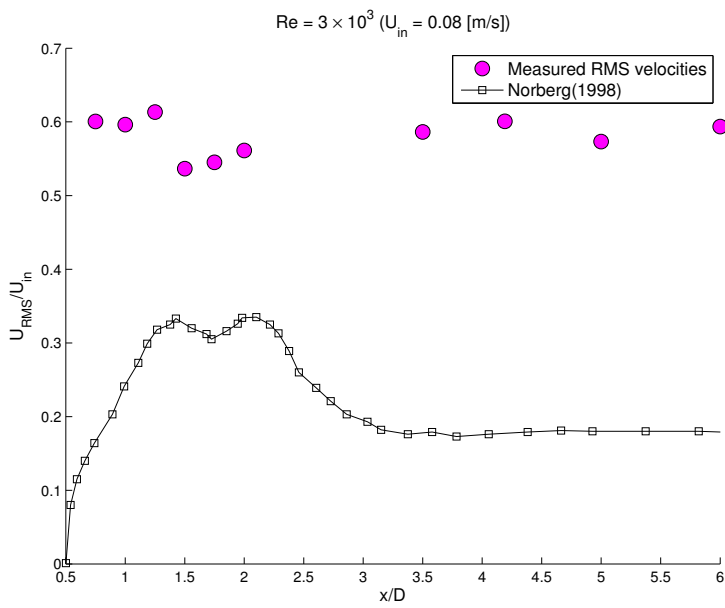


Figure 4.7: RMS velocity at points along the centerline of the wake, 260 mm above the lower edge of the cylinder at $Re = 3 \times 10^3$. Comparison with Norberg (1998)

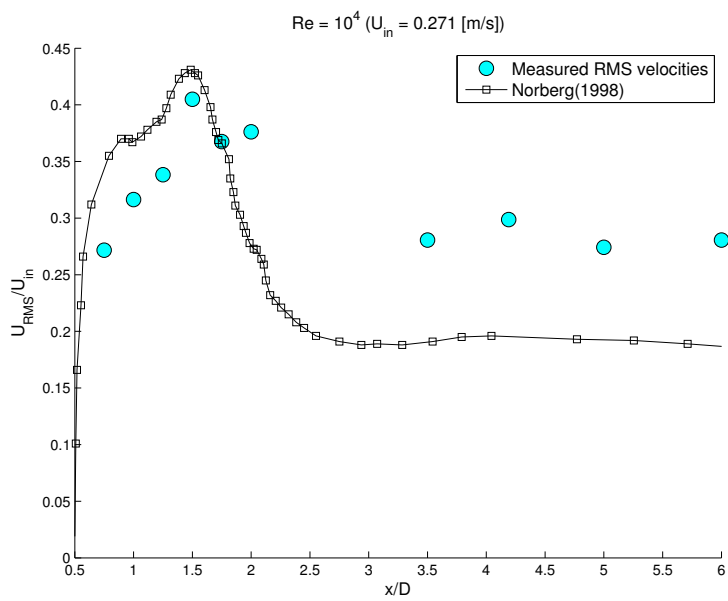


Figure 4.8: RMS velocity at points along the centerline of the wake, 260 mm above the lower edge of the cylinder at $Re = 10^4$. Comparison with Norberg (1998)

4.1.4 Velocities along the span

From Section 2.1.5 it is known that the velocity varies along the span of the cylinder due to 3D effects and the free end. The last test therefore aimed to see how large the vertical velocity variations were. The velocities were measured from the bottom of the tank along the span of the cylinder with intervals of 10 mm towards the surface of the tank. The uppermost measurement point was at 470 mm above the lower edge of the cylinder, due to the limitation of the traversing movement. This was done at 1, 3 and 5 diameters from the downstream edge of the cylinder, and the results are shown in Figure 4.9.

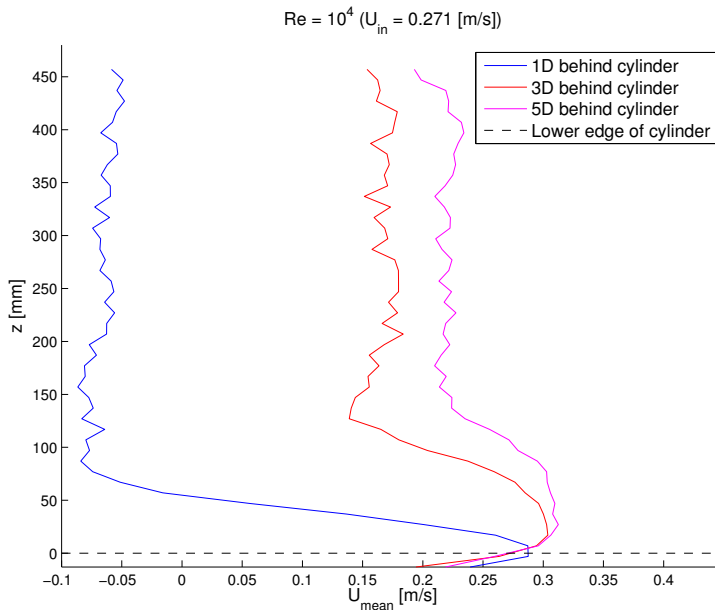


Figure 4.9: Mean velocity distribution along the span of the cylinder, measured 1, 3 and 5 diameters behind the cylinder at $Re = 10^4$

As expected, the mean velocity is clearly accelerated near the floor of the tank because of the narrow gap between the tank floor and the cylinder. One diameter behind the cylinder this effect seems to be present at the first 100 mm of the cylinder, while at 5 diameters behind the cylinder there is a substantial mean

velocity increase at approximately the first 150 mm. Above this, the mean velocity is more stable, and it can be assumed that the floor-cylinder effects are not significant there. This confirms that the vertical position of 260 mm above the lower edge of the cylinder is a reasonable position for further measurements aiming to avoid as many disturbances as possible.

4.1.5 Frequency shifting error

From the LDV verification tests, it can be concluded that the mean velocities from the LDV probe are relatively close to the reference values. The RMS velocities however were not close to the reference values. Also, the accuracy decreased with decreasing incoming flow velocity.

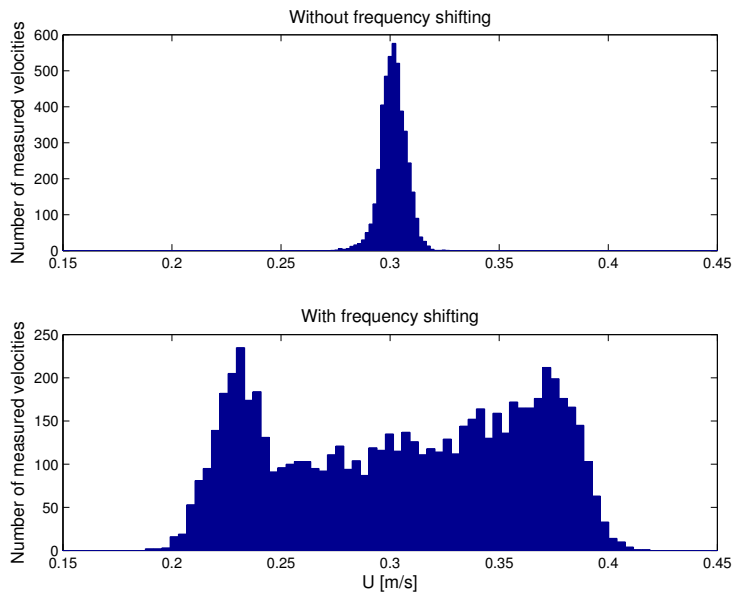


Figure 4.10: Histogram comparison between empty tank velocities without and with frequency shifting on

The cause of the erroneous LDV results is believed to be the mechanical frequency shifting device. To confirm this, three minute empty tank measurements were carried out with and without frequency shifting. Figure 4.10 shows how two

different empty tank measurements taken with and without frequency shifting under the same conditions are distributed in a histogram. Without frequency shifting, the velocities are distributed closely around the mean value as expected. However, when the frequency shifting is on, the velocity registrations are distributed over a larger range of velocities with two distinct peaks on each side of the mean velocity. The mean velocity was 1.3% larger with frequency shifting than without. The reason for the change in the velocity distribution is believed to be that the frequency shifting device was not capable of keeping a constant rotational speed. The LDV supplier was consulted regarding this error, but the problem was not solved.

It was decided to carry on with the measurements in the main experiment nevertheless due to lack of other means to measure the velocities (PIV were available at the CWT, but this would be too time consuming within the time limitations set for this thesis). It is although important to note that the accuracy stated by the manufacturer (given in Appendix B.3) is believed to be lowered due to this. This is especially the case for the RMS velocity, where the RMS velocity at best can be used as an indication of the relative strength of the wake turbulence between the different cylinder models.

4.2 Velocity in the wake of cylinders covered by marine fouling

In the first wake velocity test, four points along the wake centerline of the smooth cylinder and the four artificially roughened cylinders were measured using LDV. Due to the aforementioned issues with noise in the raw signal during the measurements – in combination with the low number of measurement points, it was not possible to achieve consistently accurate measurements. The results are therefore not presented or discussed here but can be found in Appendix C.

In the second LDV test the number of points measured along the wake centerline was increased, and to ensure reliable values, measurement points with a low average data rate and/or a low SNR were discarded.

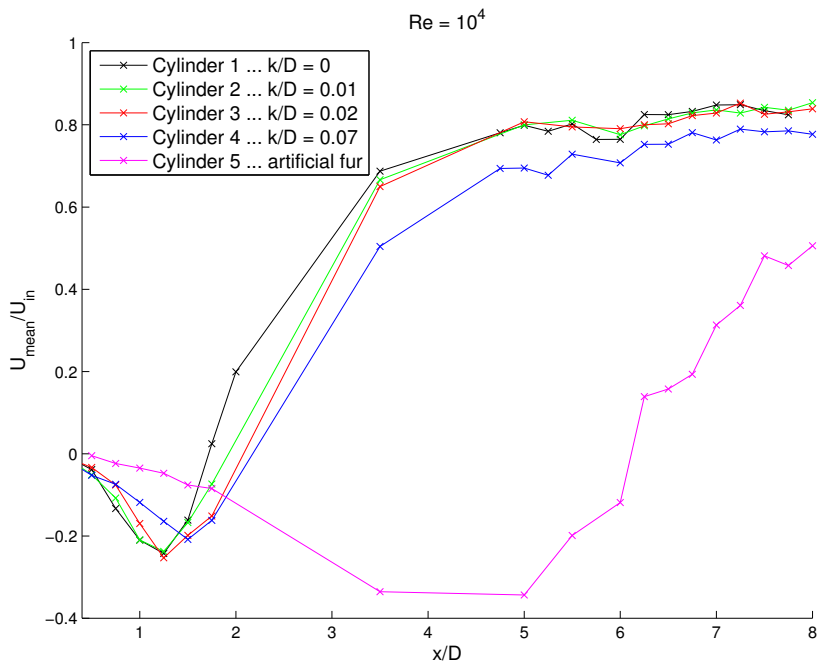


Figure 4.11: Streamwise mean velocity in the wake at $Re = 10^4$ for the five cylinder models

A comparison between the five cylinder models at $Re = 10^4$ is given in Figure 4.11. The mean velocity is given as a fraction of the incoming flow velocity (U_{mean}/U_{in}), and it can be seen that the mean velocity behind Cylinder 2 ($k/D = 0.01$) and Cylinder 3 ($k/D = 0.02$) does not deviate significantly from the results for the smooth Cylinder 1. For Cylinder 4 ($k/D = 0.07$), the mean velocity is noticeably higher than the smooth cylinder in the near wake, while it is lower from approximately two diameters and outwards. This trend can also be observed partially for the other two hard-fouling cylinders until three diameters behind the cylinder. For Cylinder 4, the minimum mean velocity is located slightly further away from the cylinder.

The cylinder with artificial fur (Cylinder 5) simulating soft marine fouling has a large deviation from the other cylinders. In the near wake the velocity is close to zero. The minimum velocity is registered five diameters from the cylinder, after where the mean velocity rapidly increases. Hence, one of the effects of soft marine fouling is that its presence significantly expands the region where the mean velocity is negative. The wake velocity profile is similar to one of a cylinder with a larger diameter. The lowest velocity is also lower than what is the case for the other cylinder models. This happens despite a low diameter increase (≈ 1 mm) and a yarn length of only about 2/3 of the diameter. From Section 2.2.2 it is known that some types of soft marine fouling can become relatively long compared to the cylinder diameter of certain structures. With the large alteration of the mean velocity introduced by the simulated soft marine fouling in this experiment, it seems realistic that structures in the ocean could be exposed to even larger wake velocity changes.

Table 4.1: U_{mean}/U_{in} at selected points along the wake

x/D	$Re = 5 \times 10^3$					$Re = 10^4$				
	1	1.5	1.75	3.5	7	1	1.5	1.75	3.5	7
Cyl. 1	-0.12	-0.17	-0.08	0.68	0.88	-0.21	-0.16	0.02	0.69	0.85
Cyl. 2	-0.08	-0.20	-0.21	0.64	0.86	-0.21	-0.17	-0.07	0.67	0.84
Cyl. 3	-0.09	-0.18	-0.11	0.61	0.90	-0.17	-0.20	-0.15	0.65	0.83
Cyl. 4	-0.12	-0.20	-0.13	0.38	0.78	-0.12	-0.21	-0.16	0.50	0.76
Cyl. 5	-0.04	-0.09	-0.12	-0.24	0.04	-0.03	-0.08	-0.08	-0.34	0.31

Figure 4.12 compares the cylinder models at $Re = 5 \times 10^3$. The same trend as for $Re = 10^4$ can be seen here. Table 4.1 gives a summary with mean velocities

for both Reynolds numbers at some selected points.

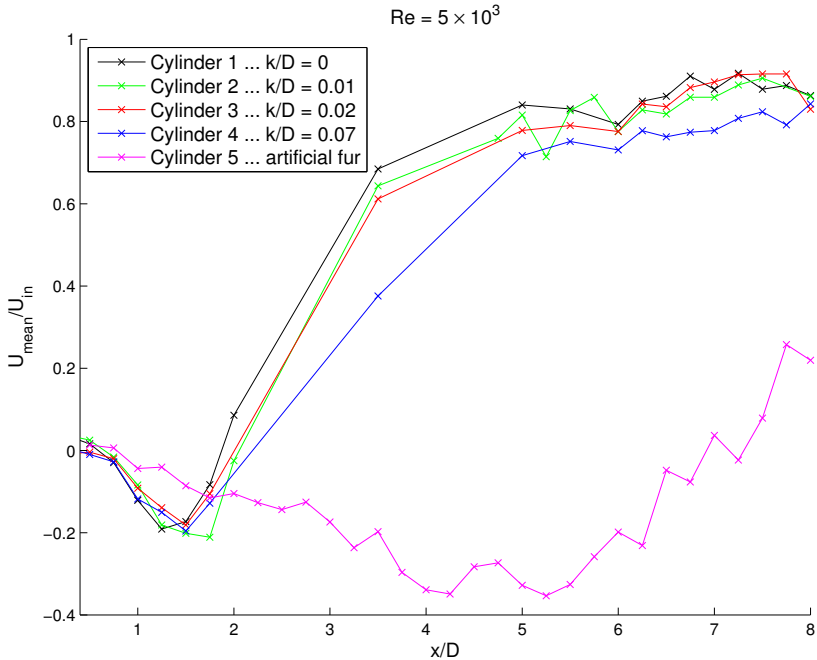


Figure 4.12: Streamwise mean velocity in the wake at $Re = 5 \times 10^3$ for the five cylinder models

The wake closure lengths of the different cylinders are presented in Table 4.2. The lengths are found by a linear approximation. As mentioned in Section 2.1.3, Norberg (1998) has previously found the wake closure length l_c of smooth cylinders to decrease with increasing Reynolds number. That is in agreement with the present findings. For the roughened cylinders, it can be seen that the values of l_c are approximately the same for Cylinder 3 and 4. This can be interpreted as an indication of a lowered dependency on Reynolds number with increasing k/D . The cylinder covered with soft marine fouling has a wake closure length approximately 3.6-3.7 times longer than the smooth cylinder. This might have implications for marine organisms in close proximity of the structure, since the environmental conditions there are significantly altered.

Table 4.2: Wake closure length l_c

	$Re = 5 \times 10^3$	$Re = 10^4$
Cyl. 1	1.9	1.7
Cyl. 2	2.0	1.9
Cyl. 3	2.1	2.1
Cyl. 4	2.2	2.2
Cyl. 5	7.0	6.1

The measured RMS velocities for all five cylinder models at $Re = 10^4$ and $Re = 5 \times 10^3$ are shown in Figures 4.13 and 4.14. As explained in Section 4.1.5 the results are inaccurate and only valid for indicating the relative magnitude of the wake velocity fluctuations. In Section 4.1.3 it was also seen that the frequency shifting error affected the RMS velocities more as the incoming flow velocity was lowered. The measurements at $Re = 10^4$ will thus give a better indication of the relative differences in RMS velocity than the measurements at $Re = 5 \times 10^3$.

In the same way as for the mean velocity results, Cylinder 5 behaves considerably different than the other four cylinders. The RMS velocity of a circular cylinder is characterized by a peak in the near wake, and this peak appears much further away from the cylinder for Cylinder 5 than for the other cylinders.

For Cylinders 1-4 the peak appears approximately 1.5-2 diameters from the rear end of the cylinder. Further away from the cylinder, all roughened cylinders lie above the smooth cylinder in RMS velocity. Generally, the trend is that the lowest relative roughness (from Cylinder 2) has a larger deviation from the smooth cylinder than the largest relative roughness (Cylinder 4). However, this trend is not identified in Figure 4.14.

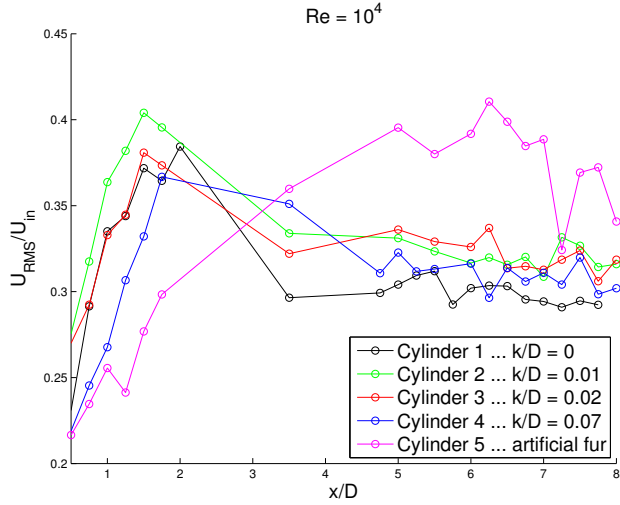


Figure 4.13: Streamwise RMS velocity in the wake at $Re = 10^4$ for the five cylinder models

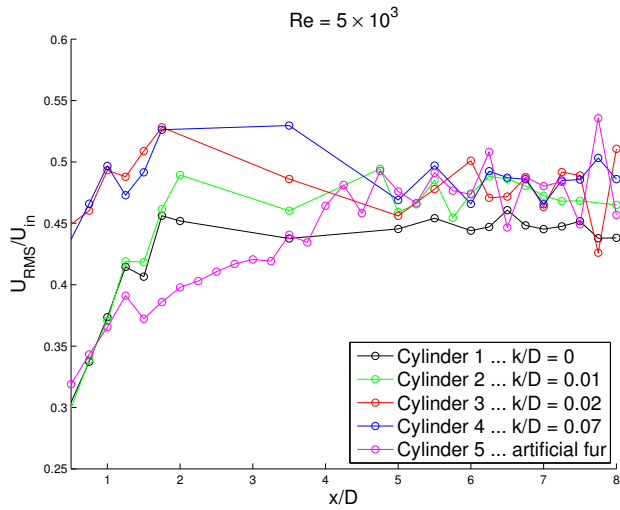


Figure 4.14: Streamwise RMS velocity in the wake at $Re = 5 \times 10^3$ for the five cylinder models

4.3 Drag coefficients

The results from the drag measurements of all five cylinder models are shown in Figure 4.15. The drag coefficients were calculated from the mean force, using Equation 7 over the length of the cylinder models. When testing the cylinder model with soft marine fouling (Cylinder 5), measurements were made both with increasing and decreasing incoming flow velocity (Plotted as a double line in the figure and indicated by “-&+” in the legend). As expected, the latter showed a slightly lower mean drag since the fur stuck around to the cylinder as the velocity was increased.

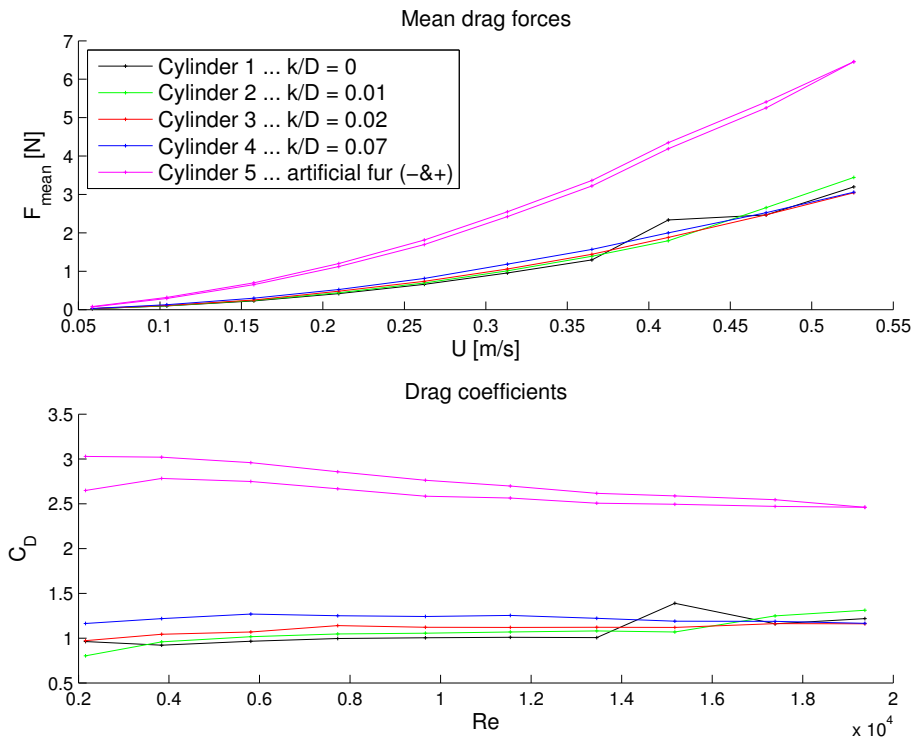


Figure 4.15: Mean drag forces and drag coefficients for each cylinder

From the measured mean drag it is clearly seen that the smooth cylinder (Cylinder 1) deviates from the trend at approximately 0.4 m/s. This is because the cylinder

Table 4.3: The velocities of where heavy vibrations were first observed

Vibrations observed at [m/s]	
Cyl. 1	0.38
Cyl. 2	0.43
Cyl. 3	0.45
Cyl. 4	0.56
Cyl. 5	Not observed

started vibrating heavily. The same happened to Cylinders 2 and 3, but at higher incoming flow velocities. This behavior was clearly observed during the measurements. Investigating the standard deviations of each time series can also give a good indication of when the vibrations started to influence the results. In Figure 4.16, the standard deviations for each time series are plotted, and it clearly shows a leap at a certain point for the first three cylinders. The velocity at the leap in standard deviation matches the velocity where the measured drag force starts to behave strangely. To verify the velocity of where the vibrations started, tests were performed where the incoming flow velocity were gradually increased until the first vibrations were observed. The results are presented in Table 4.3 and clearly matches the leaps in standard deviation.

The cylinder model and its connection to the load cell were intentionally made relatively stiff to avoid large oscillatory motions. However, the connection between the tank and the cylinder supporting frame was clearly not stiff enough in the in-line direction. The reason for the heavy vibrations therefore seems to have been that as the flow reached a certain velocity, the vortex shedding frequency coincided with the natural frequency of the cylinder supporting frame. Since the vibrations were caused by an external factor and not by the cylinder itself, the drag measurements affected by heavy vibrations have to be taken as erroneous.

For the smooth reference cylinder $C_D \approx 1$ for all measured Reynolds numbers. This corresponds well with reference values from the literature (See Appendix D).

The drag coefficient of Cylinder 2 ($k/D = 0.01$) is larger than the drag coefficient of Cylinder 1 for all non-vibrating measurements except at the lowest Reynolds number. In the region between 4×10^3 and 1.3×10^4 , the results show a nearly constant drag coefficient for Cylinders 1, 2, 3 ($k/D = 0.02$), and 4 ($k/D = 0.07$).

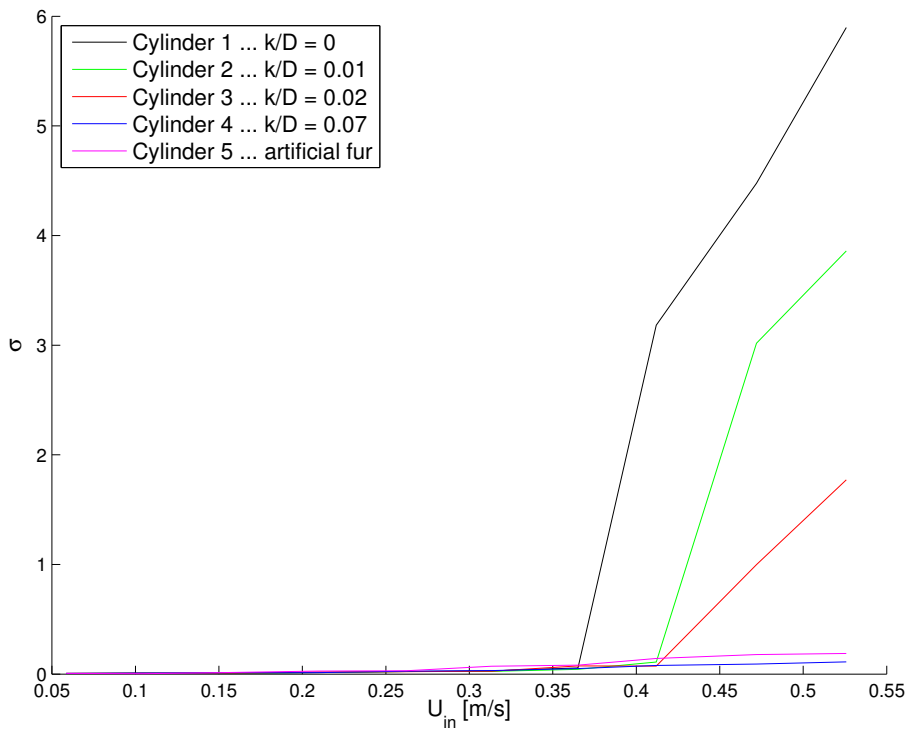


Figure 4.16: Standard deviations from each drag measurement time series

Table 4.4 compares the increase in drag coefficient caused by hard marine fouling at $Re = 9.66 \times 10^3$. It is clear that even at a low relative roughness, the drag increase is not negligible.

Table 4.4: Increase in drag coefficient caused by the presence of hard marine fouling at $Re = 9.66 \times 10^3$

	k/D	C_D	% increase
Cylinder 1	0	1.00	
Cylinder 2	0.01	1.06	6
Cylinder 3	0.02	1.12	12
Cylinder 4	0.07	1.24	24

None of the cylinder models experienced a drop in the drag coefficient (drag crisis) as the incoming flow velocity was increased. For Cylinder 1, it was known that the drag crisis would appear at a Reynolds number of approximately 10^5 (Figure 2.5). From there it is known from Section 2.1.6 an increase in surface roughness will lead to drag crisis at lower Reynolds numbers. It is also known that increasing the surface roughness decreases the magnitude of the drag coefficient drop, until the drag crisis disappears for heavily roughened cylinders. The cylinder models used in this experiment are in the same relative roughness range as Miller (1977) used in the experiments described in Figure 2.6, where no drag crisis appeared. It can thus be concluded that all cylinders are either below the critical Reynolds number regime and/or too heavily roughened for the drag crisis to appear.

The artificial fur covering Cylinder 5 caused the drag coefficient to be increased to 2.5-3. This large increase in drag is in agreement with the findings from the LDV tests, where the streamwise mean wake velocity was reduced in a significantly larger region than what was the case for the smooth cylinder. A cylinder exposed to soft marine fouling absorbs more energy from the current than a smooth cylinder, and this manifests as an increase in forces and a decrease in wake velocity.

For Cylinder 5, it could be of interest to investigate if the artificial soft marine fouling represented the same drag increase as an increase in diameter of a smooth cylinder. In other words; investigate if an equivalent smooth cylinder diameter can be found. From the expression for the drag coefficient (Equation 7), it is known that the drag force increases with the velocity squared. Power law

regression (in MS Excel) gave the results presented in Table 4.5 (Plot can be found in Appendix E).

Table 4.5: Power law regression analysis on the drag of cylinder covered with soft marine fouling. $y = ax^m$

	a	m	R^2
Increasing velocity	24.772	1.9716	0.99727
Decreasing velocity	25.716	2.0334	0.99702

The regression analysis shows that the drag of Cylinder 5 is approximately proportional to the velocity squared. Since the decreasing and increasing velocity cases most likely represents the two extremes of how soft marine fouling is aligned around a cylinder, it seems like a good approximation to assume the drag force to be proportional to the velocity squared for Cylinder 5 as well.

Assuming the drag coefficient to be approximately equal to 1, it is possible to calculate the "diameter increase" caused by soft marine fouling. At 0.2 m/s, the equivalent diameter is:

$$F_D = \frac{1}{2} \rho D L C_D U^2 = a U^2$$

$$\Rightarrow D = \frac{a}{\frac{1}{2} \rho L C_D}$$

$$a = 24.772 \Rightarrow D = 0.099 \text{ m}$$

$$a = 25.716 \Rightarrow D = 0.103 \text{ m}$$

Hence, the soft marine fouling-covered cylinder with a diameter of 0.042 m can be represented approximately as a 0.10 m smooth cylinder.

The results show that the diameter increase, which is the main focus in the rules and guidelines described in Section 2.4 is not the only parameter to consider when designing offshore structures. The presence of soft fouling – which does not necessarily appear as a large diameter increase in a visual survey, could lead to a large increase in forces and significantly alter the wake velocities.

Time series plots from the drag measurements can be found in Appendix F.

4.4 Flow visualization

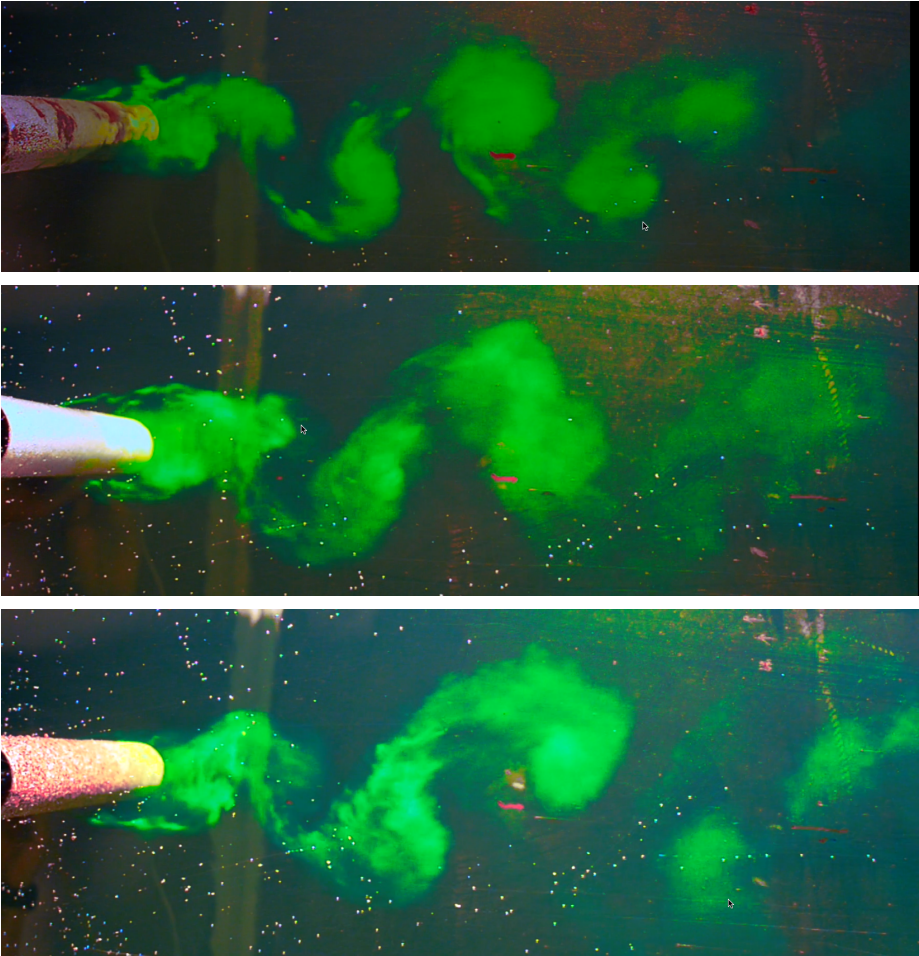


Figure 4.17: Flow visualization, Cylinders 1, 2 and 3 (in that order)

Figures 4.17 and 4.18 show visualizations of the wake flow for all cylinder models at an incoming flow velocity of 0.21 m/s. The most apparent feature from the visualizations is found when comparing Cylinder 5 with the other cylinders. The vortex shedding is established significantly further away from the rear part of the

cylinder for Cylinder 5. This supports the findings from the LDV investigation where the wake closure length was found to be significantly larger for Cylinder 5 than for the other cylinders.



Figure 4.18: Flow visualization, Cylinders 4 and 5 (in that order)

Another apparent feature is the increased dye mixing caused by the roughened cylinders. The dye is clearly less dissolved and flows more smoothly behind Cylinder 1, compared to what is the case behind for instance Cylinder 4. Increased mixing indicates increased wake fluctuations – supporting the data in Figure 4.13.

A frame-by-frame investigation of the video record from the visualization gave an approximation of the vortex shedding frequencies. The findings are presented in Table 4.6, where T_v is the vortex shedding period estimated from the video. The Strouhal number is calculated with the smooth cylinder diameter.

Table 4.6: Strouhal numbers for the five cylinder models from flow visualization. $U = 0.21$ m/s

	k/D	T_v	St
Cylinder 1	0	1.05	0.19
Cylinder 2	0.01	1.25	0.16
Cylinder 3	0.02	1.25	0.16
Cylinder 4	0.07	1.25	0.16
Cylinder 5	soft	1.90	0.11

Cylinder 5 has a significantly lower Strouhal number than Cylinder 1, which supports the equivalent diameter theory established in Section 4.3. The cylinders covered by hard marine fouling (Cylinders 2-4) have approximately the same Strouhal number, lower than Cylinder 1. This can also be seen by comparing the length of two subsequent vortices for e.g. Cylinder 1 and 3 in Figure 4.17; the distance between two subsequent vortices is larger for Cylinder 3 than for Cylinder 1. Since the flow is below the critical Reynolds number regime, the boundary layer is still laminar and the separation points have not moved. The lowered vortex shedding frequency for Cylinders 2-4 is believed to be caused by a slight increase in the distance between the separation points due to the surface irregularities. This is more evident for Cylinder 5; Figure 4.18 clearly shows that the vortices are shed further away from each other than for Cylinder 1.

It is important to note that a video record investigation such as this only provides an estimate of the actual vortex shedding frequency. It is difficult to measure the exact time between two vortices since the dye could be dispersed differently from one vortex to another. Nevertheless, the investigation gave solid evidence that the vortex shedding is altered due to the presence of marine fouling. As mentioned in Section 2.3.2, a change in the vortex shedding frequency could have large implications when it comes to fatigue life. In addition, "lock-in" will occur at other frequencies than what would be the case for the structure when it was new.

Appendix G provides detailed images from the visualization.

5 Conclusion

The effects of marine fouling on circular cylinders have been assessed through a literature study and an experimental investigation. The mean drag of different cylinder models has been successfully measured, and in addition LDV measurements in the wake have been carried out. In conclusion, marine fouling causes problems for a wide range of industries, and the distribution of the fouling organisms are dependent on many factors. In the areas around the North Sea, blue mussels are often dominant in the upper depth zone, while smaller organisms such as hydroids, tube worms and barnacles often are found below the mussel zone. The distribution is however dependent on many factors and could differ a lot from one location to another.

Marine fouling is in most cases divided into two categories; hard and soft. In general, hard marine fouling leads to an increased diameter and surface roughness on ocean structures, and the fouling was simulated in this investigation by glueing sand/gravel of different grain sizes onto cylinder models. Modeling soft marine fouling is challenging, but artificial fur was found to move similar to real fouling in current and was used in this experiment.

Five different cylinder models were tested at subcritical Reynolds numbers with regards to mean drag and wake velocity in a flume tank. The diameter of all cylinders was 0.042 m. Tests prior to the experiment revealed an error in the LDV probe which caused the RMS velocities to be erroneous, while the mean velocities were correct.

The mean drag was found to increase with increasing surface roughness. Cylinders covered with hard marine fouling with relative roughnesses of $k/D = 0.01$, $k/D = 0.02$ and $k/D = 0.07$, had a drag increase of 6, 12 and 24 % respectively, compared to a smooth cylinder at $Re = 10^4$.

The mean drag on the cylinder covered by artificial soft marine fouling had a drag 2.5-3 times larger than the drag of a smooth cylinder at Reynolds between 0.2×10^3 and 1.9×10^4 . The mean drag of the cylinder was found to be approximately proportional to the velocity squared, in the same way as for smooth cylinders. From this, the equivalent smooth cylinder diameter was found to be 0.10 m.

The LDV system was programmed to run along the centerline of the wake, between 0.5 and 8 diameters from the rear end of the cylinder. Only the streamwise velocity was measured, at Reynolds numbers of 5×10^3 and 10^4 .

The presence of hard marine fouling was found to slightly alter the mean velocity distribution in the wake. Increasing surface roughness was found to increase the mean velocity near the cylinder, while it decreased the mean velocity further away from the cylinder. Increasing surface roughness gave a minor increase in the wake closure length. The results indicated that the Reynolds number dependence of the wake closure length was decreased as the surface roughness was increased.

Soft marine fouling altered the wake velocity significantly. The wake closure length was found to be 6-7 diameters, compared to 1.7-1.9 diameters for the smooth cylinder. This was expected due to the large increase in mean drag for the same cylinder.

The wake visualizations supported the findings from the LDV tests. In addition, the Strouhal numbers obtained from the visualizations were found to be altered due to the marine fouling. The introduction of hard marine fouling on a smooth cylinder changed the Strouhal number from approximately 0.19 to 0.16. No relation between relative roughness and Strouhal number was found. For the cylinder covered by soft marine fouling, the Strouhal number was approximately 0.11.

In summary, it is important to note the type of marine fouling when conducting a fouling survey – since soft marine fouling could significantly alter forces and flow beyond what could be expected just from its apparent diameter increase. Hard marine fouling also alters both the drag and the wake structure, but less significantly than soft marine fouling.

6 Further work

In this section, the experience gained from the project is used to suggest improvements for future marine fouling investigations.

- **Measure wake turbulence**

Due to the frequency shifting error in the LDV probe described in Section 4.1.5, it was not possible to obtain accurate values of the streamwise RMS velocity in the wake. By either repairing the probe or by attempting the same measurements with a different properly working probe, these statistical values can be obtained. Another attempt is to use particle image velocimetry (PIV) – with which the whole velocity field in the wake can be measured. Acquiring the RMS velocity data would be of large interest e.g. for marine ecologists – since it would provide a better understanding of the wake turbulence and of how larvae is dissipated from fouled structures.

- **Perform the second experiment**

As explained in Section 3, a test setup was made for an experiment that was not carried out. This was due to a broken load cell which could not be fixed or replaced within the time limitation of this project. The setup consisted of cylinder models spanned horizontally across the CWT, with the forces measured on a small section in the middle of the cylinder. This would give several advantages when it comes to eliminating 3D effects. The setup also allows for using the CWT with a closed lid, avoiding free surface interactions.

The sensor planned for use in this experiment was an ATI IP68 Nano17 force/torque sensor (shown in Figure 6.2), capable of measuring the force and torque in three dimensions. The main advantage of this sensor is that it is waterproof, and it is small enough to be fitted inside the cylinder model (the diameter of the sensor is just 20.1 mm). Specifications and drawings of the sensor can be found in Appendix B.2.

Five circular cylinder models covered with the same artificial marine fouling as in the preliminary experiment (described in Table 3.4) were made for



Figure 6.1: Test rig made for the second experiment



Figure 6.2: The ATI IP68 Nano17 force sensor. From ATI brochure given in Appendix B.2

Table 6.1: Specifications for the second experiment

Cylinder diameter [mm]	60
Cylinder thickness [mm]	4
Aspect ratio (L/D)	9.83
Total cylinder span [mm]	590
Test section length [mm]	50

the test. Since this setup is less sensitive to boundary disturbances, it allows for an increase in the cylinder diameter. It was decided to increase the cylinder model diameter to 60 mm, to be able to cover a slightly larger range of Reynolds numbers. Specifications for the test setup are given in Table 6.1, and the test rig is shown in Figure 6.1.

The advantage of this test setup as compared to the experiment carried out in this thesis is that it would provide accurate measurements of the drag, lift and Strouhal number and decrease the effect of disturbances.

- **Better modeling of marine fouling**

In this project marine fouling has been quantified by using one parameter; the relative roughness. By for instance using a 3D scanner, the shape of the artificial marine roughness could have been documented. Although this would not improve the actual modeling of marine fouling, but it would make it easier to use the data for comparison with real marine fouling.

A more accurate modeling of marine fouling could be achieved if in addition the shape of the fouling could be simulated. This is a difficult task in such a small scale as in the CWT, but in a larger scale it could be possible.

- **Marine fouling survey data**

Since marine fouling differs so much from one location to another, it would be of great benefit to have a larger amount of marine fouling data from actual offshore sites. Although the offshore wind industry regularly inspects

the piles of the wind turbines, not many of the reports are found to be publicly available. Cooperation with the industry and performing detailed surveys should be a priority for future investigations.

References

- Achenbach, E. (1971). Influence of surface roughness on the cross-flow around a circular cylinder. *J. Fluid Mech.*, 46:321–335.
- Achenbach, E. and Heinecke, E. (1981). On vortex shedding from smooth and rough cylinders in the range of Reynolds numbers 6×10^3 to 5×10^6 . *J. Fluid Mech.*, 109:239–251.
- Almeida, E., Diamantino, T. C., and de Sousa, O. (2007). Marine paints: The particular case of antifouling paints. *Progress in Organic Coatings*, 59:2–20.
- Applied University Research, Inc. (n.d.). General LDV brochure. <http://www.aurinc.com/images/generalLDVbroc.pdf>. [Accessed 05.04.2014].
- Baarholm, R. (2007). Recent MARINTEK activities on assessment of vortex-induced vibrations. Presentation from MARINTEK do Brasil Opening Seminar http://sintef.org/project/MARINTEK%20Seminar/Presentations/VIV%20Highlights_Baarholm_rev01.pdf. [Accessed 04.02.2014].
- Baarholm, R. and Skaugset, K. (2008). Modelling and characterization of artificial marine growth. In *Proceedings of the ASME 27th International Conference on Offshore Mechanics and Arctic Engineering*.
- Boutier, A. (2012). *Laser velocimetry in fluid mechanics*. Waves series. Wiley-ISTE, 1 edition.
- Brujjs, M. C. M. (2010). Survey of marine fouling on turbine support structures of Offshore Windfarm Egmond aan Zee. Technical report, KEMA Technical and Operational Services.
- Busscher, H. J. and van der Mei, H. C. (2000). Initial microbial adhesion events: mechanisms and implications. In Allison, D., Gilbert, P., Lappin-Scott, H., and Wilson, M., editors, *Society for General Microbiology, Symposium 59: Community Structure and Co-operation in Biofilms*, pages 25–32. Cambridge University Press.
- Dürr, S. and Thomason, J. C., editors (2010). *Biofouling*. Wiley-Blackwell.
- EESI (2010). Fact sheet - offshore wind energy. http://www.eesi.org/files/offshore_wind_101310.pdf. [Accessed 15.09.2013].

- Efunda website (n.d). Laser doppler flow theory. http://www.efunda.com/designstandards/sensors/laser_doppler/laser_doppler_flow_theory.cfm. [Accessed 20.03.2014].
- EWEA (2011). Wind in our sails: The coming of Europe's offshore wind energy industry. http://www.ewea.org/fileadmin/ewea_documents/documents/publications/reports/23420_Offshore_report_web.pdf. [Accessed 15.09.2013].
- EWEA (2013). The European offshore wind industry - key trends and statistics 1st half 2013. http://www.ewea.org/fileadmin/files/library/publications/statistics/EWEA_OffshoreStats_July2013.pdf. [Accessed 15.09.2013].
- Fage, A. and Warsap, J. (1929). *The effects of turbulence and surface roughness on the drag of a circular cylinder*, volume No. 1283 of *Reports and memoranda*. H.M. Stationery Office.
- Frostick, L. E., McLelland, S. J., and Mercer, T., editors (2011). *Users guide to physical modelling and experimentation: Experience of the HYDRALAB network*. CRC Press/Balkema, Leiden, The Netherlands.
- International Maritime Organization (2002). Focus on IMO - Anti-fouling systems. [http://www.imo.org/KnowledgeCentre/ReferencesAndArchives/FocusOnIMO\(Archives\)/Pages/default.aspx](http://www.imo.org/KnowledgeCentre/ReferencesAndArchives/FocusOnIMO(Archives)/Pages/default.aspx). [Accessed 29.10.2013].
- ISO 19901-1 (2005). *Petroleum and natural gas industries - Specific requirements for offshore structures, Part 1: Metocean design and operating considerations*. International Organization for Standardization, Geneva, Switzerland.
- Jusoh, I. and Wolfram, J. (1996). Effects of marine growth and hydrodynamic loading on offshore structures. *Jurnal Mekanikal*, 1.
- Koehl, M. A. R. (2007). Mini review: Hydrodynamics of larval settlement into fouling communities. *Biofouling*, 23(5):357–368.
- Langhamer, O. (2005). *Man-made offshore installations: Are marine colonisers a problem or an advantage?* Introductory research essay, Department of Animal Ecology, Evolutionary Biology Centre, Uppsala University.
- Langhamer, O. (2009). *Wave energy conversion and the marine environment: colonization patterns and habitat dynamics*. PhD thesis, Uppsala University.

- Langhamer, O. (2010). *Colonization of blue mussels (Mytilus Edulis) on offshore wave power installations*, chapter 12. Nova Science Publishers, Inc.
- Measurement Science Enterprise Inc. (2013). Measurement science enterprise inc. website. http://measurementsci.com/about_LDV-LDA3.html. [Accessed 01.11.2013].
- Measurement Science Enterprise Inc. (n.d.). 2D miniLDV brochure. http://measurementsci.com/papers/2DminiLDV_brochure.pdf. [Accessed 01.11.2013].
- Miller, B. L. (1977). The hydrodynamic drag of roughened circular cylinders.
- Norberg, C. (1998). Ldv-measurements in the near wake of a circular cylinder. In *Advances in understanding of bluff body wakes and vortex-induced vibration*. ASME Fluids Engineering Division.
- NORSOK N-003 (2007). *Actions and action effects*. NORSOK Standard, 2 edition.
- Oldfield, D. G. (1980). *Appraisal of marine fouling on offshore structures*. CIRIA.
- Panton, R. L. (1996). *Incompressible flow*, chapter 14, page 387. John Wiley and Sons, Inc., 2 edition.
- Schlichting, H. and Gersten, K. (2000). *Boundary layer theory*, volume 8. Springer-Verlag.
- Steen, S. (2012). TMR7 Experimental methods in marine hydrodynamics. Lecture notes.
- Sumer, B. and Fredsøe, J. (1997). *Hydrodynamics around cylindrical structures*. Advanced series on ocean engineering. World Scientific.
- White, F. M. (2008). *Fluid mechanics*. McGraw-Hill.
- Wholmersley, P. and Picken, G. B. (2003). Long-term dynamics of fouling communities found on offshore installations in the north sea. *J. Mar. Biol. Ass. U.K.*, 83:897–901.
- Wolfram, J. and Theophanatos, A. (1990). Marine roughness and fluid loading. *Environmental forces on offshore structures and their prediction*, 26:137–258.

- Woods Hole Oceanographic Institute (1952). *Marine fouling and its prevention*, chapter 11. U.S Naval Institute, Annapolis, Maryland.
- Yebra, D. M., Kiil, S., and Dam-Johansen, K. (2004). Antifouling technology - past, present and future steps towards efficient and environmentally friendly antifouling coatings. *Progress in Organic Coatings*, 50:75–104.
- Zdravkovich, M. M. (1997). *Flow around circular cylinders: Volume I and II*. Flow Around Circular Cylinders: A Comprehensive Guide Through Flow Phenomena, Experiments, Applications, Mathematical Models, and Computer Simulations. OUP Oxford.

A Task description

The task description written by supervisor Prof. Dag Myrhaug is given in the next two pages.



NTNU Trondheim
Norwegian University of Science and Technology
Department of Marine Technology – Group of Marine Structures

MASTER THESIS IN MARINE TECHNOLOGY

SPRING 2014

FOR

STUD. TECHN. EIRIK LEIKVOLL NEDREBØ

EXPERIMENTAL INVESTIGATION OF MARINE FOULING ON PILES IN CURRENTS

Bio fouling (or marine fouling) on ship hulls, piles, and elements of marine structures is a major economic and technical problem worldwide. In recent decades the development and growth of the offshore oil and gas industry has led to increased interest in and studies on bio fouling in the marine environment.

This experimental investigation will focus on the effects of marine fouling on piles in steady flows, and the student shall:

1. Give a background of the investigation.
2. Give a theoretical background.
3. Describe the experimental methods including description of the test facility with test set-up and test procedure.
4. Present results and discussion.

The work scope may prove to be larger than initially anticipated. Subject to approval from the supervisor, topics may be deleted from the list above or reduced in extent.

In the thesis the candidate shall present his personal contribution to the resolution of problem within the scope of the thesis work.

Theories and conclusions should be based on mathematical derivations and/or logic reasoning identifying the various steps in the deduction.

The candidate should utilize the existing possibilities for obtaining relevant literature.

The thesis should be organized in a rational manner to give a clear exposition of results, assessments, and conclusions. The text should be brief and to the point, with a clear language. Telegraphic language should be avoided.

The thesis shall contain the following elements: A text defining the scope, preface, list of contents, summary, main body of thesis, conclusions with recommendations for further work, list of symbols and acronyms, reference and (optional) appendices. All figures, tables and equations shall be numerated.

The supervisor may require that the candidate, in an early stage of the work, present a written plan for the completion of the work. The plan should include a budget for the use of computer and laboratory resources that will be charged to the department. Overruns shall be reported to the supervisor.

The original contribution of the candidate and material taken from other sources shall be clearly defined. Work from other sources shall be properly referenced using an acknowledged referencing system.

The thesis shall be submitted:

- Signed by the candidate
- The text defining the scope included
- In bound volume(s)
- Drawings and/or computer prints which cannot be bound should be organized in a separate folder.

Advisors: PhD student Pierre-Yves Henry
Professor Dag Myrhaug

Deadline: 10.06.2014



Dag Myrhaug
Supervisor

B Instrumentation drawings and specifications

B.1 Load cell data sheet

PW4MC3...

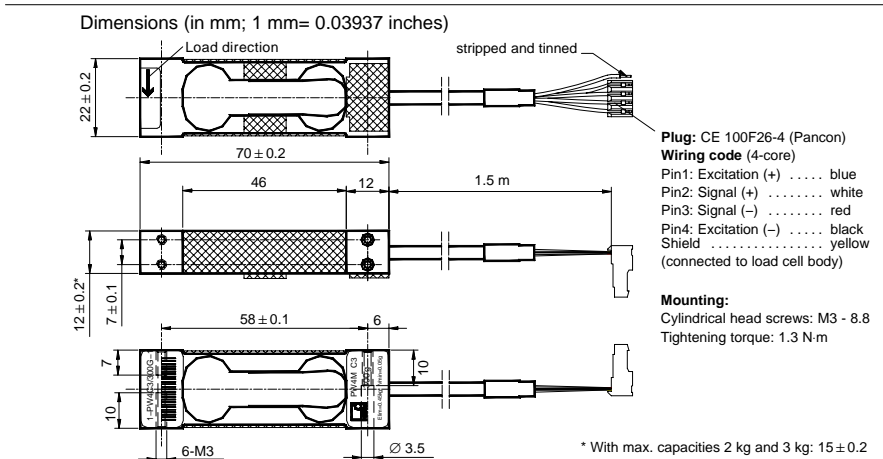
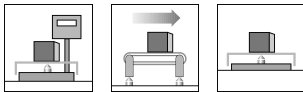
Single point load cells

Data Sheet



Special features

- For determining small masses
- Small size
- Accuracy class C3 with OIML-R60 test report
- Off center load compensated
- Degree of protection IP65 according to IEC 529
- Shielded connection cable



B2224-2.1 en



Specifications

Type		PW4MC3...			
Order-No.		1-PW4C3/300G-1	1-PW4C3/500G-1	1-PW4C3/2KG-1	1-PW4C3/3KG-1
Accuracy class ¹⁾		C3			
Maximum number of load cell intervals (n_{LC})		3000			
Maximum capacity ²⁾ (E_{max})	g/kg	300	500	2	3
Minimum LC verification interval (v_{min})	g	0.05	0.1	0.2	0.5
Temperature effect on zero balance (TK_0)	% of C_N / 10 K	0.0233	0.0280	0.0140	0.0233
Max. platform size	mm	200 x 200			
Sensitivity (C_N)	mV/V	1.0 ± 0.1		2.0 ± 0.2	
Zero signal		0 ± 0.1			
Temperat. effect on sensitivity (TK_C) ³⁾	% of C_N / 10 K	± 0.0175 ± 0.0117			
Temperature range: +20 ... +40 °C [68...104 °F] -10 ... +20 °C [14...68 °F]					
Hysteresis error (d_{hy}) ³⁾		± 0.0150			
Non-linearity (d_{lin}) ³⁾		± 0.0150			
Minimum dead load output return (MDLOR)	% of C_N	± 0.0245			
Off center load error ⁴⁾		± 0.0233			
Input resistance (R_{LC})	Ω	380 ± 38			
Output resistance (R_0)		380 ± 38			
Reference excitation voltage (U_{ref})		5			
Nominal range of excitation voltage (E_U)	V	1 ... 8			
Insulation resistance (R_{is}) at 100 V _{DC}	GΩ	> 2			
Nominal temperature range (E_T)		-10 ... +40 [+14...+104]			
Operating temperature range (E_{UW})	°C [°F]	-10 ... +50 [+14...+122]			
Storage temperature range (E_{st})		-25 ... +70 [-13...+158]			
Limit load (E_L) ^{*)}	% of E_{max}	150			
*) at max. eccentricity	mm	100			
Lateral load limit (E_{lq}), static	%	200			
Breaking load (E_{d})	of E_{max}	> 300			
Deflection at E_{max} (s_{nom}), approx.	mm	< 0.4			
Weight, without cable (G), approx.	kg	0.07			
Degree of protection according to IEC529		IP65			
Material:	Measuring element Coating Cable sheath	Aluminum Silicone rubber PVC			

¹⁾ In accordance to OIML R60 with $P_{LC} = 0.7$

²⁾ Max. eccentric load according to OIML R76

³⁾ The data for Non-linearity (d_{lin}), Hysteresis error (d_{hy}) and Temperature effect on sensitivity (TK_C) are typical values. The sum of these data meets the requirements according to OIML R60.

⁴⁾ According to OIML R76

Modifications reserved.
All details describe our products in general form only. They are not to be understood as express warranty and do not constitute any liability whatsoever.

B2224-2.1 en

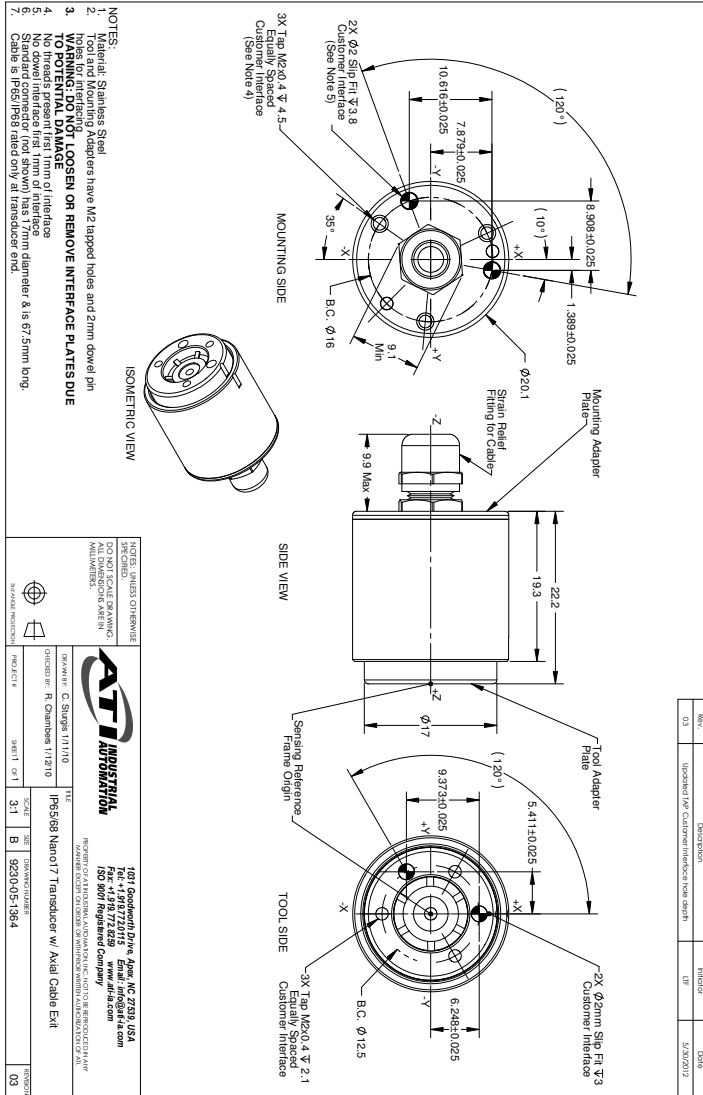
Hottinger Baldwin Messtechnik GmbH

Im Tiefen See 45, D-64293 Darmstadt, Germany
Tel.: +49 6151 803-0 Fax: +49 6151 803 9100
Email: support@hbm.com Internet: www.hbm.com



measurement with confidence

B.2 Force/Torque sensor



4.3 Nano17 (Includes IP65/IP68 Versions)

4.3.1 Calibration Specifications (excludes CTL calibrations)

Note:

The outer body of the IP65 and the IP68 versions of the Nano17 are electrically floating from the rest of the system. If the transducer signal has additional noise, it may be necessary to electrically connect the transducer body to the case of the F/T system.

US (English)

Calibration	Fx,Fy	Fz	Tx,Ty	Tz	Fx,Fy	Fz	Tx,Ty	Tz
US-3-1	3 lbf	4.25 lbf	1 lbf-in	1 lbf-in	1/1280 lbf	1/1280 lbf	1/8000 lbf-in	1/8000 lbf-in
US-6-2	6 lbf	8.5 lbf	2 lbf-in	2 lbf-in	1/640 lbf	1/640 lbf	1/4000 lbf-in	1/4000 lbf-in
US-12-4	12 lbf	17 lbf	4 lbf-in	4 lbf-in	1/320 lbf	1/320 lbf	1/2000 lbf-in	1/2000 lbf-in
SENSING RANGES				RESOLUTION				

SI (Metric)

Calibration	Fx,Fy	Fz	Tx,Ty	Tz	Fx,Fy	Fz	Tx,Ty	Tz
SI-12-0.12	12 N	17 N	120 Nmm	120 Nmm	1/320 N	1/320 N	1/64 Nmm	1/64 Nmm
SI-25-0.25	25 N	35 N	250 Nmm	250 Nmm	1/160 N	1/160 N	1/32 Nmm	1/32 Nmm
SI-50-0.5	50 N	70 N	500 Nmm	500 Nmm	1/80 N	1/80 N	1/16 Nmm	1/16 Nmm
SENSING RANGES				RESOLUTION				

These system resolutions quoted are the effective resolution after dropping eight counts of noise. The effective resolution can be improved with filtering. NOTE: Applied loads must be within range in each of the six axes for the F/T sensor to measure correctly.

4.3.2 CTL Calibration Specifications

US (English)

Calibration	Fx,Fy	Fz	Tx,Ty	Tz	Fx,Fy	Fz	Tx,Ty	Tz
US-3-1	3 lbf	4.25 lbf	1 lbf-in	1 lbf-in	1/640 lbf	1/640 lbf	1/4000 lbf-in	1/4000 lbf-in
US-6-2	6 lbf	8.5 lbf	2 lbf-in	2 lbf-in	1/320 lbf	1/320 lbf	1/2000 lbf-in	1/2000 lbf-in
US-12-4	12 lbf	17 lbf	4 lbf-in	4 lbf-in	1/160 lbf	1/160 lbf	1/1000 lbf-in	1/1000 lbf-in
SENSING RANGES				RESOLUTION				

SI (Metric)

Calibration	Fx,Fy	Fz	Tx,Ty	Tz	Fx,Fy	Fz	Tx,Ty	Tz
SI-12-0.12	12 N	17 N	120 Nmm	120 Nmm	1/160 N	1/160 N	1/32 Nmm	1/32 Nmm
SI-25-0.25	25 N	35 N	250 Nmm	250 Nmm	1/80 N	1/80 N	1/16 Nmm	1/16 Nmm
SI-50-0.5	50 N	70 N	500 Nmm	500 Nmm	1/40 N	1/40 N	1/8 Nmm	1/8 Nmm
SENSING RANGES				RESOLUTION				

US (English)

Calibration	Fx,Fy	Fz	Tx,Ty, Tz	Fx,Fy	Fz	Tx,Ty, Tz
US-3-1	±3 lbf	±4.25 lbf	±1 lbf-in	0.3 lbf/V	0.425 lbf/V	0.1 lbf-in/V
US-6-2	±6 lbf	±8.5 lbf	±2 lbf-in	0.6 lbf/V	0.85 lbf/V	0.2 lbf-in/V
US-12-4	±12 lbf	±17 lbf	±4 lbf-in	1.2 lbf/V	1.7 lbf/V	0.4 lbf-in/V
Analog Output Range			Analog ±10V Sensitivity‡			

SI (Metric)

Calibration	Fx,Fy	Fz	Tx,Ty, Tz	Fx,Fy	Fz	Tx,Ty, Tz
SI-12-0.12	±12 N	±17 N	±120 Nmm	1.2 N/V	1.7 N/V	12 Nmm/V
SI-25-0.25	±25 N	±35 N	±250 Nmm	2.5 N/V	3.5 N/V	25 Nmm/V
SI-50-0.5	±50 N	±70 N	±500 Nmm	5 N/V	7 N/V	50 Nmm/V
Analog Output Range			Analog ±10V Sensitivity‡			

Counts Value

Calibration	Fx, Fy, Fz	Tx, Ty, Tz	Fx, Fy, Fz	Tx, Ty, Tz
US-3-1 / SI-12-0.12	5120 / lbf	32000 / lbf-in	1280 / N	256 / Nmm
US-6-2 / SI-25-0.25	2560 / lbf	16000 / lbf-in	640 / N	128 / Nmm
US-12-4 / SI-50-0.5	1280 / lbf	8000 / lbf-in	320 / N	64 / Nmm
Tool Transform Factor	0.0016 in/lbf		0.05 mm/N	
Counts Value – US (English)			Counts Value – SI (Metric)	

CTL resolutions are typical. System resolutions quoted are the effective resolution after dropping eight counts of noise. The effective resolution can be improved with filtering. NOTE: Applied loads must be within range in each of the six axes for the F/T sensor to measure correctly.

‡ ±5V Sensitivity values are double the listed ±10V Sensitivity values.

CAUTION:



IP68 Nano17 Fz as a Function of Submersion Depth:

When submerged, IP68 transducers exhibit a decrease in Fz range related to the submersion depth. This loss is the result of pressure-induced preloading on the transducer. The preload can be masked by biasing the transducer at the depth prior to applying the load to be measured. The following estimates are for room temperature fresh water at seal level.

IP68 Nano17	US	Metric
Fz preload at 1m depth	-0.50 lb	-2.22 N
Fz preload at other depths	-0.15 lb/ft × depthInFeet	-2.22 N/m × depthInMeters

4.3.3 Nano17 Physical Properties
US (English)

Single-Axis Overload	
Fxy	±56 lbf
Fz	±110 lbf
Txy	±14 lbf-in
Tz	±16 lbf-in
Stiffness (Calculated)	
X-axis & Y-axis forces (Kx, Ky)	4.7x10 ⁴ lb/in
Z-axis force (Kz)	6.5x10 ⁴ lb/in
X-axis & Y-axis torque (Ktx, Kty)	2.1x10 ³ lbf-in/rad
Z-axis torque (Ktz)	3.4x10 ³ lbf-in/rad
Resonant Frequency (Measured, non-IP version)	
Fx, Fy, Tz	7200 Hz
Fz, Tx, Ty	7200 Hz
Physical Specifications	
Weight*	0.02 lb
Diameter*	0.67 in
Height*	0.57 in

SI (Metric)

Single-Axis Overload	
Fxy	±250 N
Fz	±480 N
Txy	±1.6 Nm
Tz	±1.8 Nm
Stiffness (Calculated)	
X-axis & Y-axis forces (Kx, Ky)	8.2x10 ⁶ N/m
Z-axis force (Kz)	1.1x10 ⁷ N/m
X-axis & Y-axis torque (Ktx, Kty)	2.4x10 ² Nm/rad
Z-axis torque (Ktz)	3.8x10 ² Nm/rad
Resonant Frequency (Measured, non-IP version)	
Fx, Fy, Tz	7200 Hz
Fz, Tx, Ty	7200 Hz
Physical Specifications	
Weight*	0.00907 kg
Diameter*	17 mm
Height*	15 mm

* Specifications include standard interface plate.

B.3 LDV brochure

2D miniLDV™

Integrated 2D miniature laser Doppler velocimeter

The 2D miniLDV incorporates two 1D probes with frequency shifting into a single unit with permanently co-located probe volumes. It is ideal for research and commercial applications. Setting up takes less than one hour because MSE's miniLDV probes require no alignment or calibration by the user.

ADVANTAGES OF THE 2D MINI-LDV:

- Self-contained
- Factory sealed
- Co-located probe volumes
- No alignment needed
- Calibration done at the factory
- Frequency shifting on both components
- No water cooling required
- Accurate measurement of fluids of varying temperature, pressure, and density
- Computer controlled 1, 2, and 3-axis traversing system
- 2D and 3D automated profile measurement
- Battery operated option
- Waterproof and temperature resistant housing option

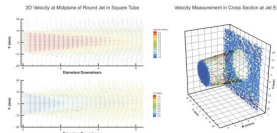
APPLICATIONS INCLUDE:

- Fluid mechanics, aerodynamics, turbulence, oceanography, and atmosphere studies
- Wind, water, oil tunnels and channels

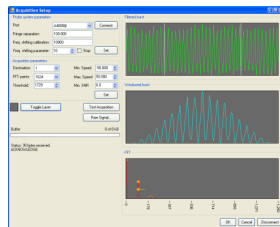


The 2D miniLDV System with 50 to 240 mm standoff is extremely compact, self contained, and permanently aligned; no calibration or alignment by the user is required. The probe contains two high power diode lasers, miniature beam shaping optics, and receiving and detection optics.

2D Flow Mapping with miniLDV™



The 2D miniLDV System includes the 2D miniLDV probe, dual Processing Engines, and a multidimensional version of MSE's Burst Processor Acquisition Manager software. With the optional computerized traverses, setting up a flow-mapping experiment for unattended acquisition is a matter of minutes, not hours.



The interface of the acquisition software complements the probe's ease of use.

MEASUREMENT SPECIFICATIONS	
Velocity range	-50 to 600 m/sec*
Repeatability	99.9%
Accuracy	99.7% or better

PROBE VOLUME	
PV dimensions (x by y by z)	Typical: 150 x 300 x 1200 μm**
Available standoff distances	50 mm, 100 mm, 150 mm and 240 mm

PROBE SPECIFICATIONS	
Probe weight	2 lbs (1kg)
Dimensions	51 x 76 x 150 mm 2 x 3 x 6 inches

LASER SPECIFICATIONS	
Laser power	2 x 130 mW
Wavelengths	658 and 785 nm
laser type	Class IIb

OPERATING PARAMETERS	
Temperature	0 to 55°C
Pressure	Atmospheric
PC requirements	Laptop or PC

OPTIONAL FEATURES	
Water proof, high pressure, and high temperature housing	
Traversing stage for profile measurements	
1-D, 2-D, and 3-D traversing systems	

POWER SUPPLY	
12 VDC Universal	

* Velocity range is a function of the fringe separation and the dynamic range. Please specify your required velocity range.

** Probe volume dimension is a function of the standoff distance

One or more of the following U.S. Patents apply: No. 6,654,102, 6,580,503, 6,608,668, 6,717,172, 6,956,230

V201111



MEASUREMENT
SCIENCE
ENTERPRISE, INC.

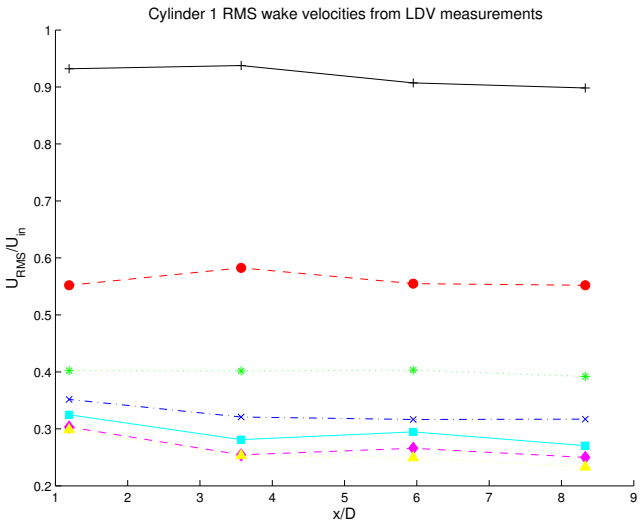
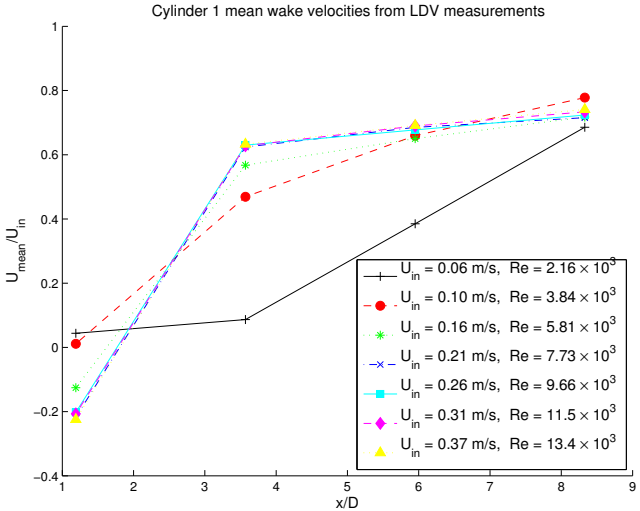
123 W. Bellevue Dr., Suite 1
Pasadena, CA 91105
USA

Info@MeasurementSci.com
Phone: +1 (626) 577 0566
Fax: +1 (626) 577 0565

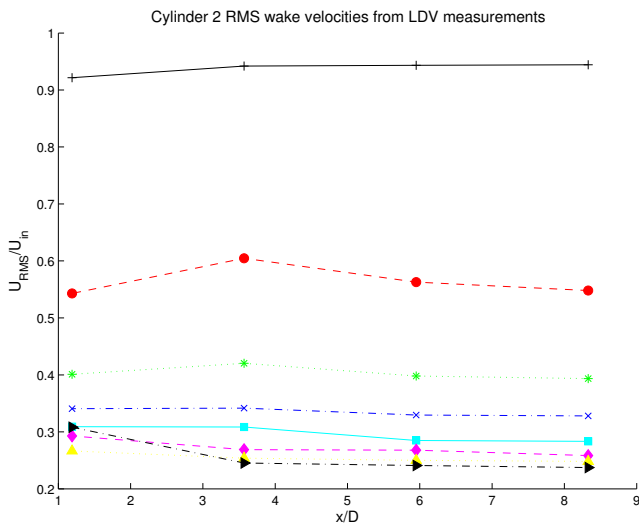
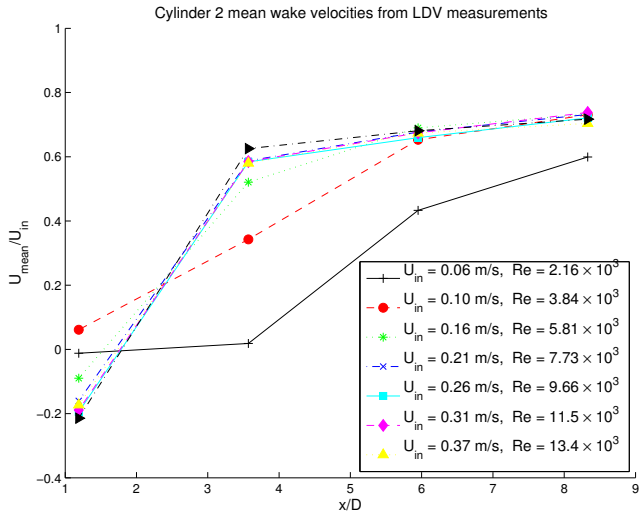
C Wake velocity results

The following pages provide the streamwise velocity results from the initial LDV tests, where four points along the centerline of the wake were measured. The results proved to be inaccurate, most likely due to noise in the raw signal.

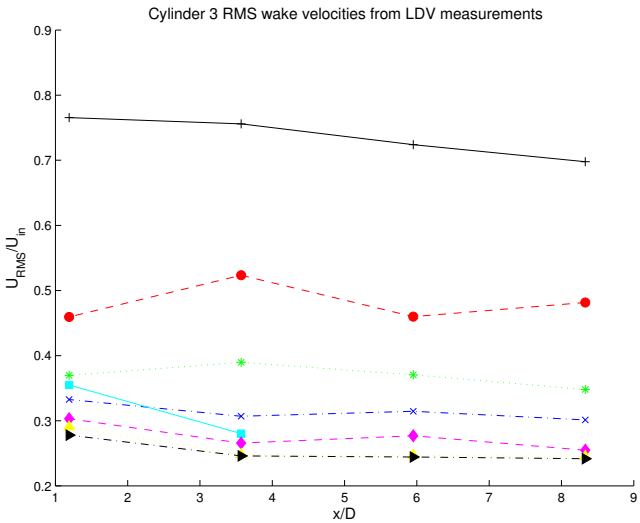
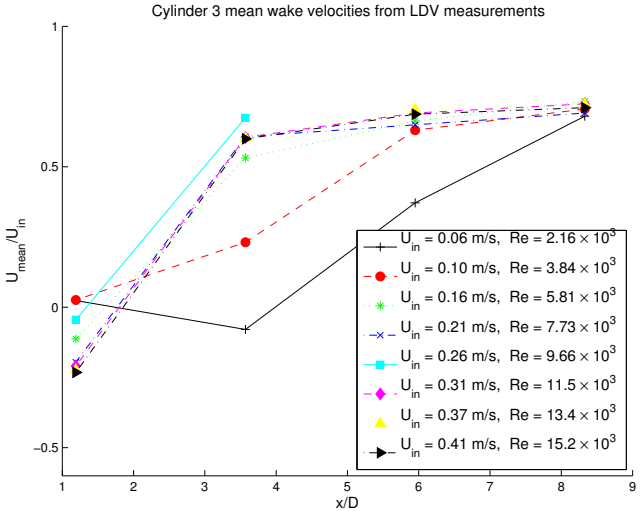
Cylinder 1 ($k/D = 0$)



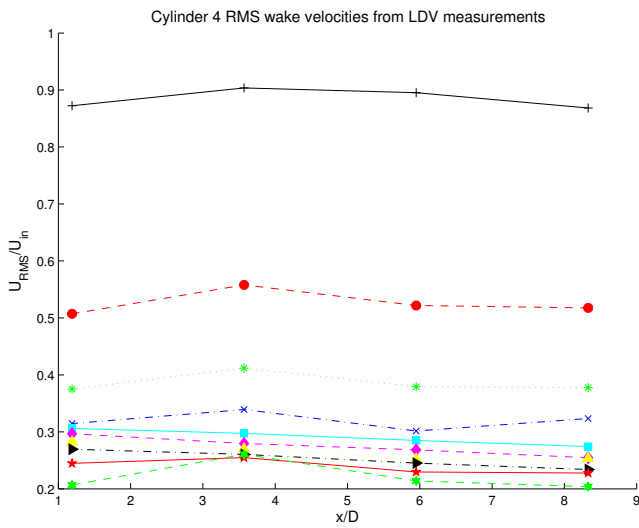
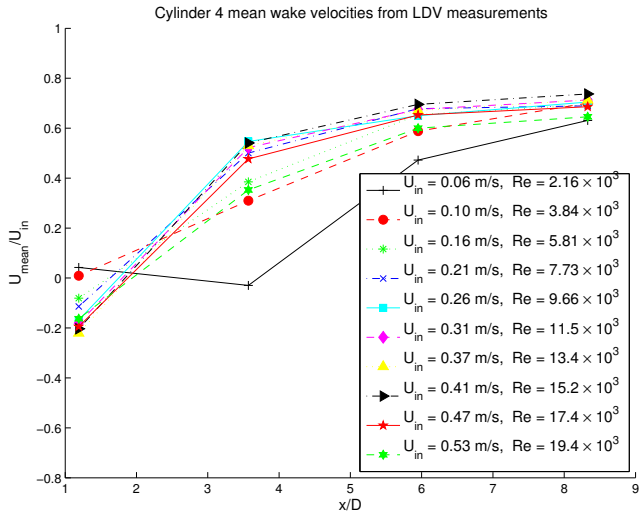
Cylinder 2 ($k/D = 0.01$)



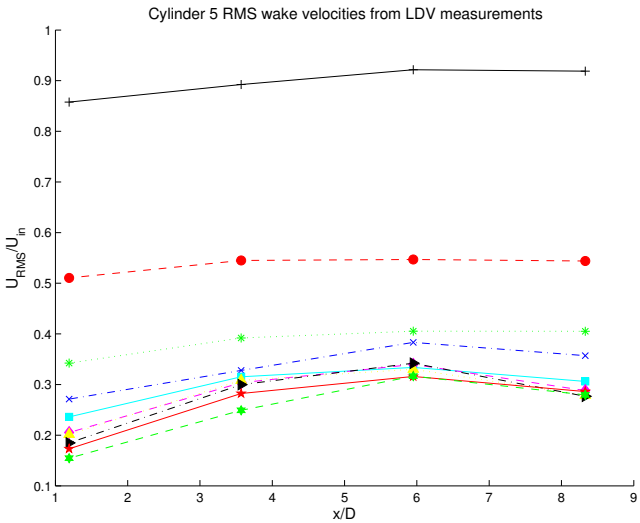
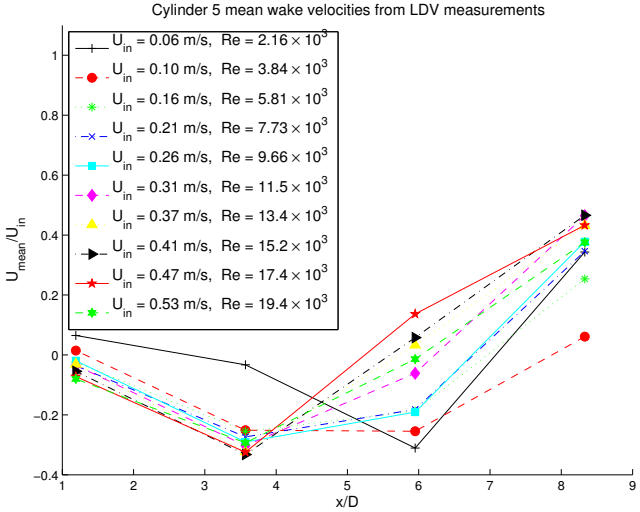
Cylinder 3 ($k/D = 0.02$)



Cylinder 4 ($k/D = 0.07$)

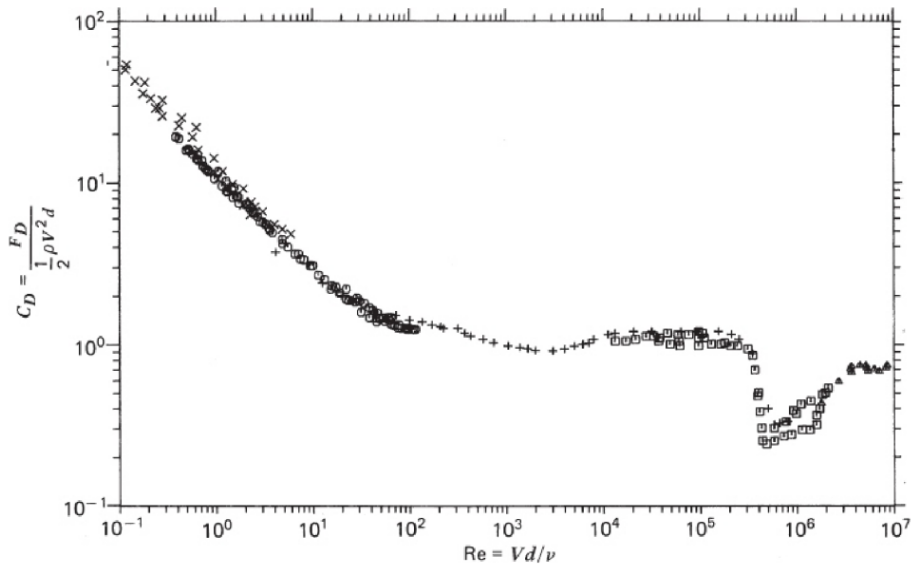


Cylinder 5 (Soft marine fouling – artificial fur)



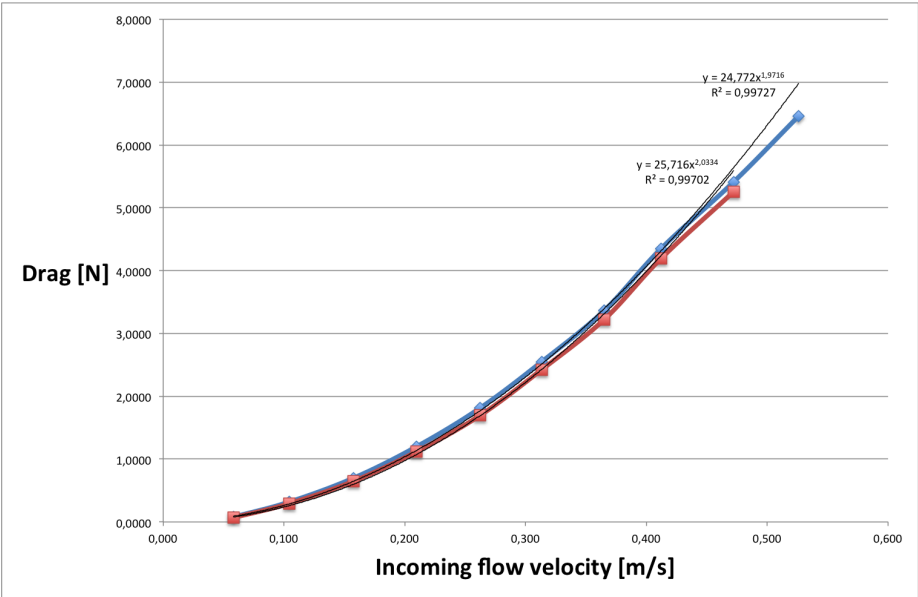
D Circular cylinder drag coefficient

This figure shows the drag coefficient for a smooth circular cylinder, taken from Panton (1996).



E Drag regression analysis

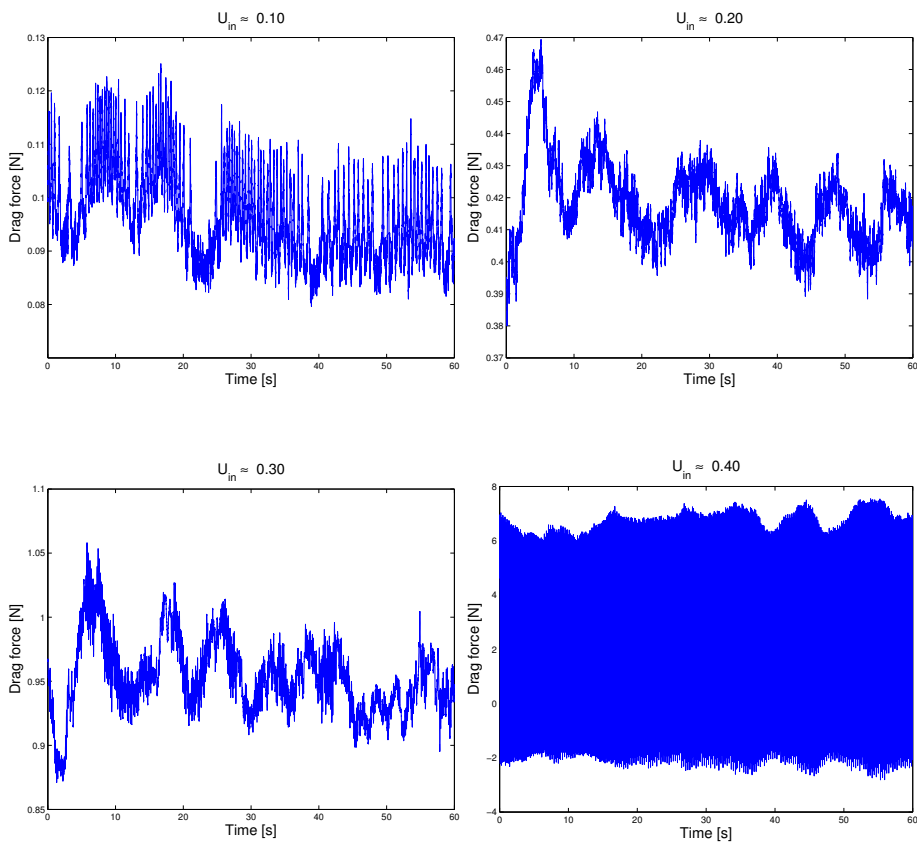
This figure shows the MS Excel power law regression plots for increasing (blue line) and decreasing (red line) incoming flow velocity on Cylinder 5.



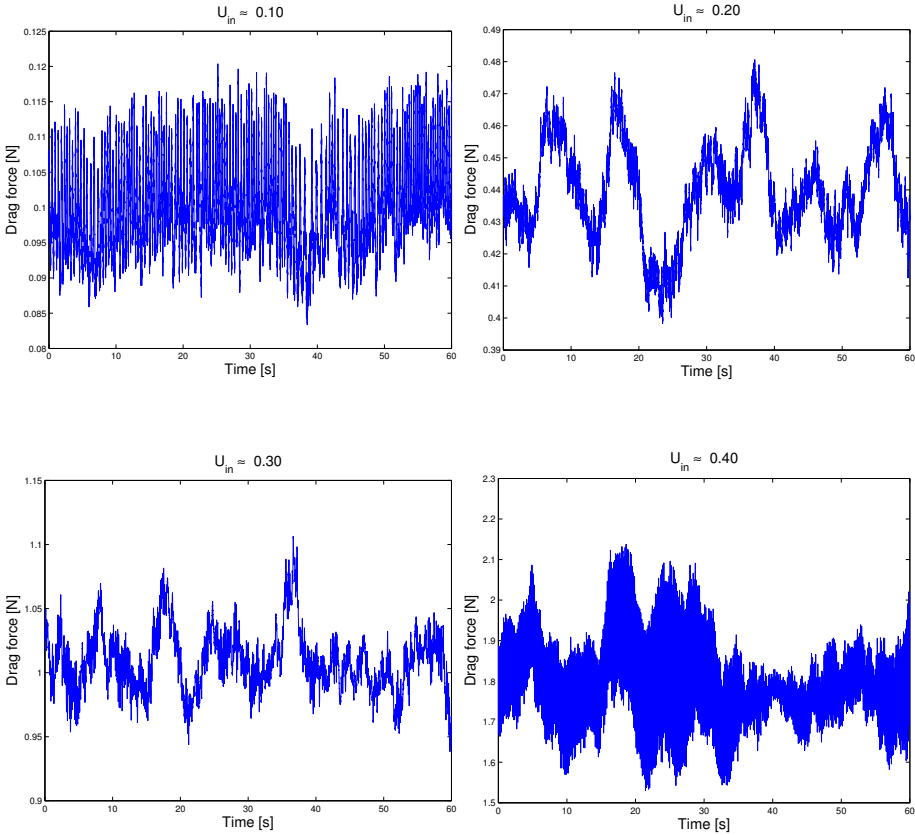
F Drag time series

The 60 second drag force time series for all cylinders at four different incoming flow velocities are given in the following pages.

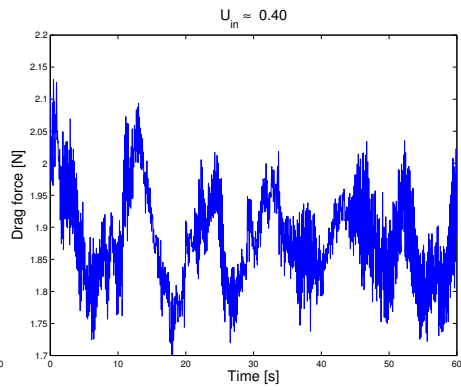
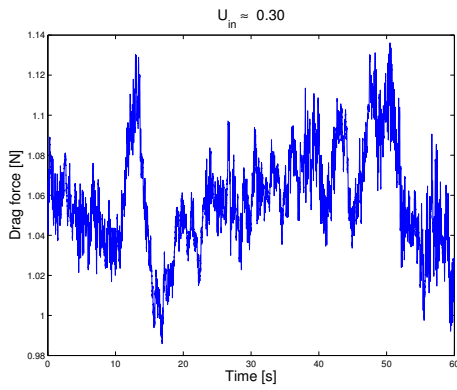
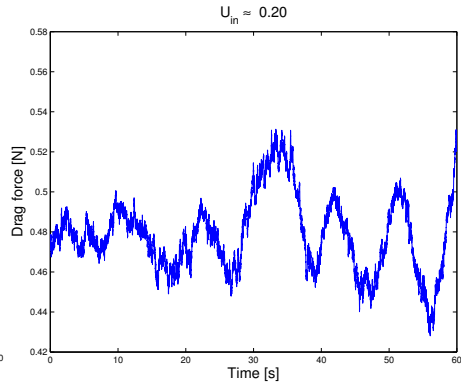
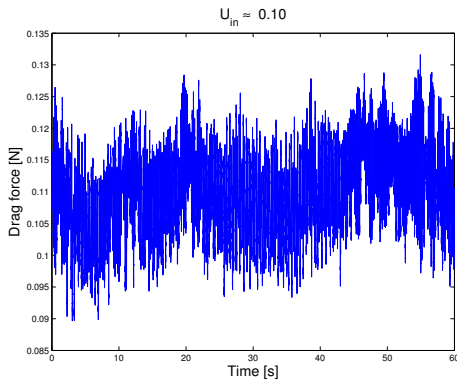
Cylinder 1 ($k/D = 0$)



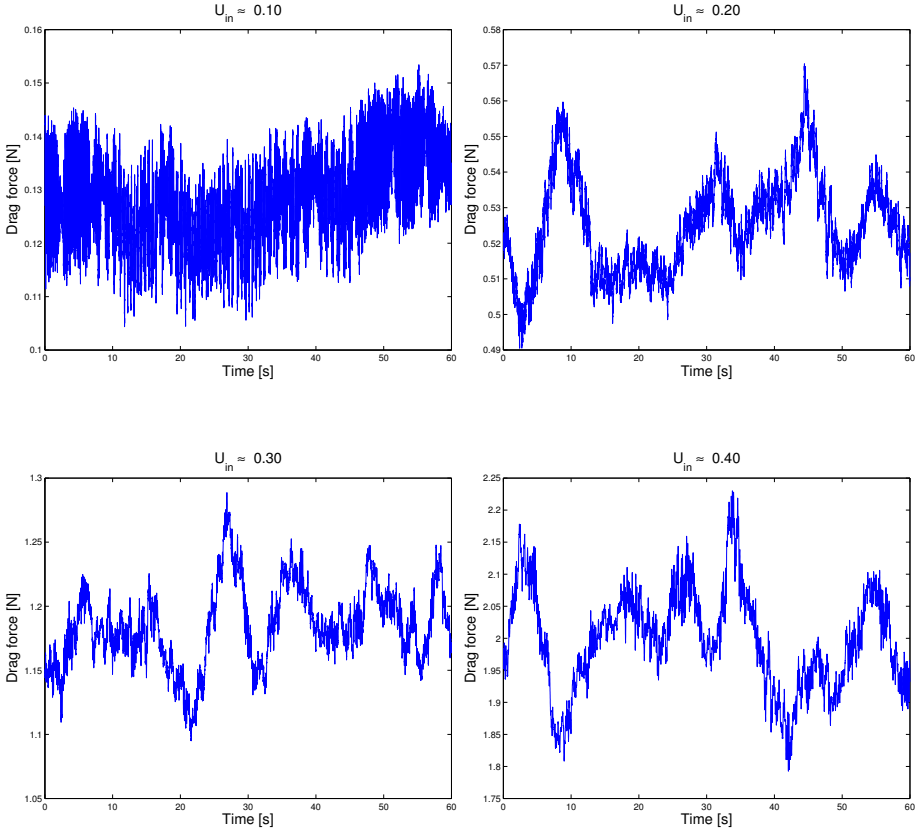
Cylinder 2 ($k/D = 0.01$)



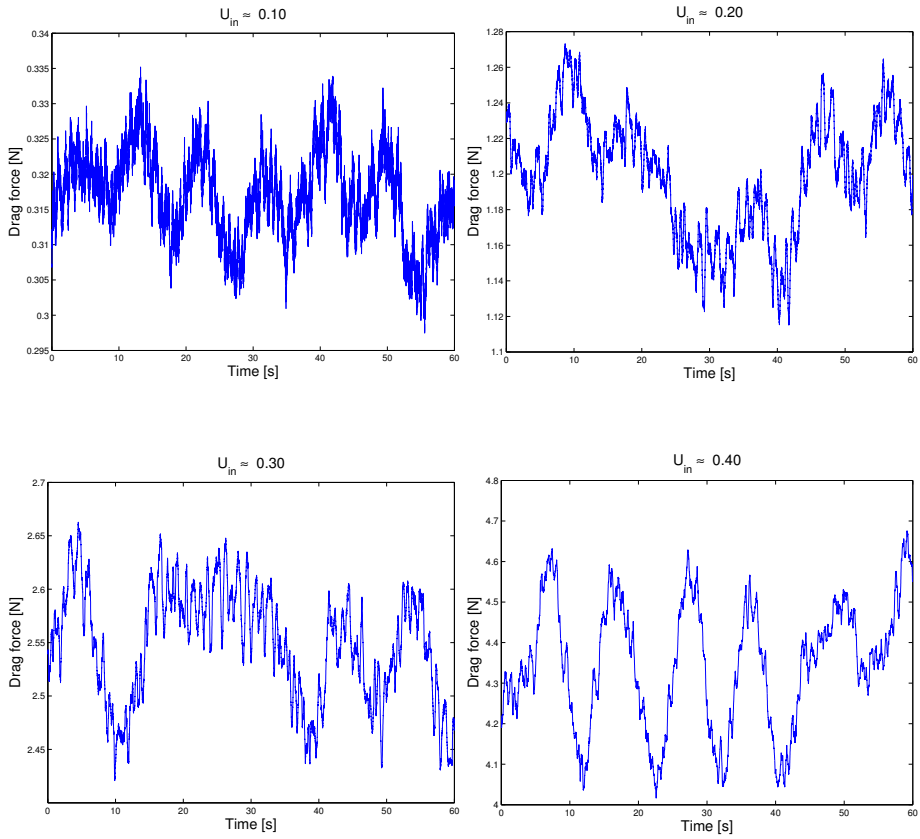
Cylinder 3 ($k/D = 0.02$)



Cylinder 4 ($k/D = 0.07$)



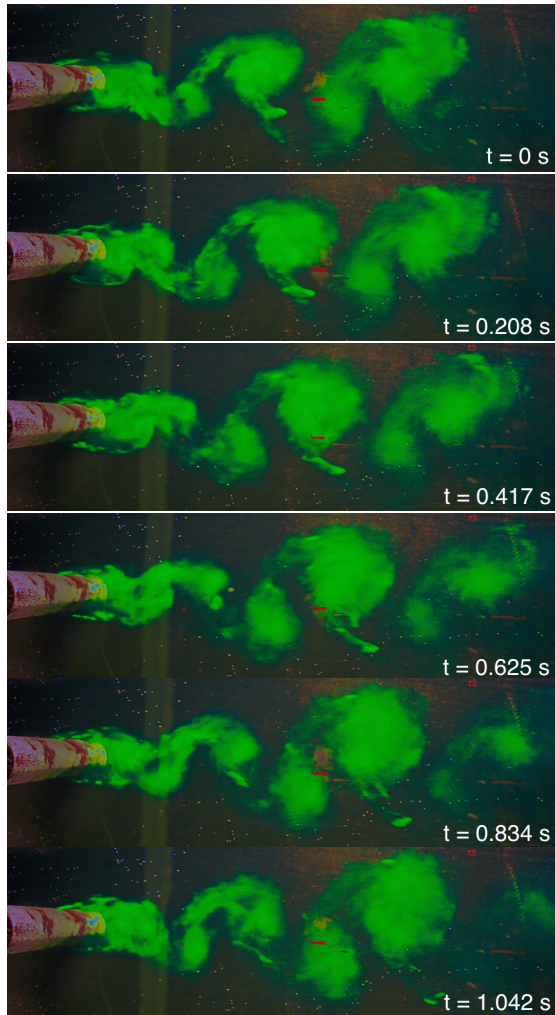
Cylinder 5 (Soft marine fouling – artificial fur)



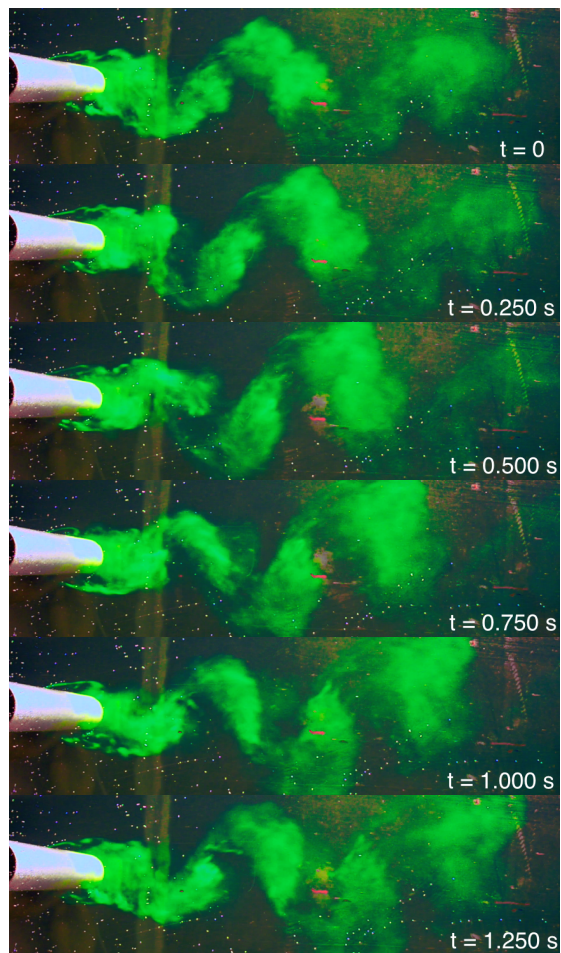
G Wake visualization

Pictures from the flow visualization are given in the following pages. Each picture is marked with the time instant it was taken (relative to the first image).

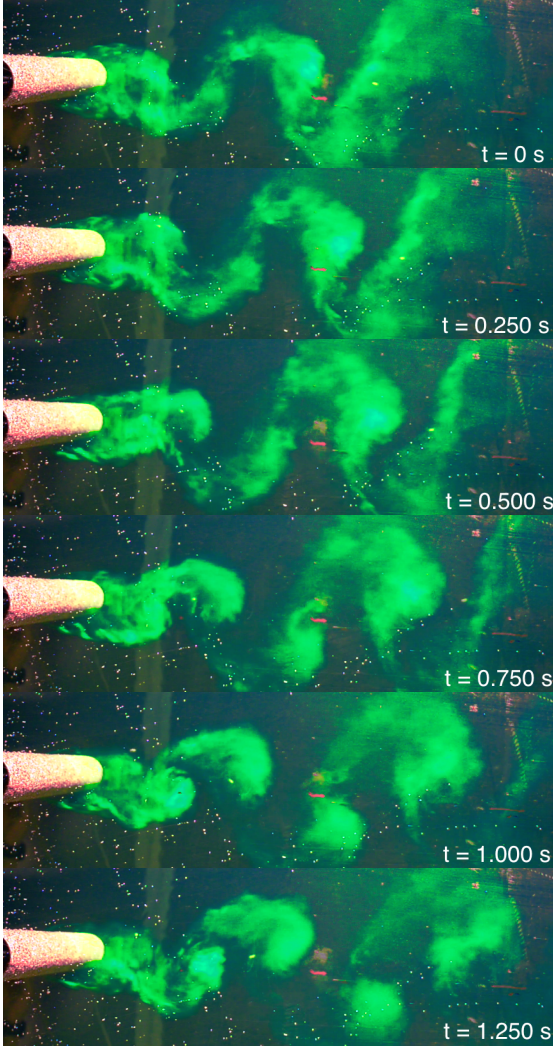
Cylinder 1 ($k/D = 0$)



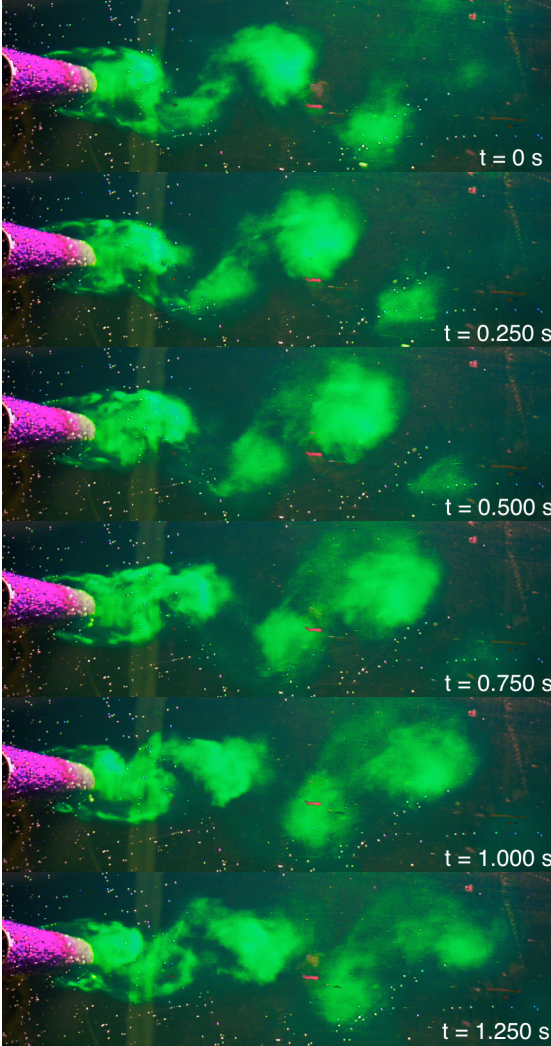
Cylinder 2 ($k/D = 0.01$)



Cylinder 3 ($k/D = 0.02$)



Cylinder 4 ($k/D = 0.07$)



Cylinder 5 (Soft marine fouling – artificial fur)

